PERGAMON

International Journal of Multiphase Flow 27 (2001) 971–1009

International Journal of Multiphase Flow

www.elsevier.com/locate/ijmulflow

Ellipsoidal particles transport and deposition in turbulent channel flows

Haifeng Zhang [a], Goodarz Ahmadi [a,*], Fa-Gung Fan [b], John B. McLaughlin [c]

[a] *Department of Mechanical and Aeronautical Engineering, Room CAMP 267, Clarkson University, Potsdam, NY 13699-5727, USA*

[b] *J.C. Wilson Center for Research and Technology, Xerox Corporation, Webster, NY 14580, USA*

[c] *Department of Chemical Engineering, Clarkson University, Potsdam, NY 13699-5705, USA*

Received 4 November 1999; received in revised form 29 October 2000

Abstract

Ellipsoidal particle transport and deposition in dilute turbulent channel flows are studied. The instantaneous fluid velocity field is generated by the direct numerical simulation (DNS) of the Navier–Stokes equation via a pseudospectral method. The particle equations of motion used include the hydrodynamic forces and torques, the shear-induced lift and the gravitational forces. Euler's four parameters (quaternions) are used for describing the time evolution of particle orientations. Ensembles of ellipsoidal particle trajectories in turbulent channel flows are generated and statistically analyzed. The results are compared with those for spherical particles and their differences are discussed. Effects of particle size and aspect ratio, turbulence near wall eddies, and the gravitational and hydrodynamic forces are studied. The DNS predictions are compared with the available experimental data and earlier sublayer model simulation results and reasonable agreements are observed.

1. Introduction

Transport and deposition of aerosol particles in turbulent flows have been the subject of intense research in the past few decades due to their numerous scientific and engineering applications. Air pollution control, pneumatic transport, coal combustion and gasification, inhalation toxicology, clean room application and microcontamination in semiconductor industry are among the areas in which the knowledge of particle dispersion and deposition plays a critical role.

* Corresponding author. Tel.: +1-315-268-2322/6586; fax: +1-315-268-6438/6695.
E-mail address: ahmadi@clarkson.edu (G. Ahmadi).

0301-9322/01/$ - see front matter
PII: S0301-9322(00)00064-1

Extensive experimental and computational studies related to particle transport in turbulent flows were reported in the literature (Hinze, 1975; Hinds, 1982; Wood, 1981a,b; Ahmadi, 1993). Papavergos and Hedley (1984) and McCoy and Hanratty (1977) reviewed the available experimental measurements of the deposition rates of particles and droplets in turbulent gas flows in vertical pipes. Correlations relating the deposition velocity to particle relaxation time and particle Schmidt numbers were suggested by Wood (1981a,b) and Papavergos and Hedley (1984). A sublayer model for particle resuspension and deposition in turbulent flows was proposed by Cleaver and Yates (1973, 1975, 1976), Fichman et al. (1988) and Fan and Ahmadi (1993).

Direct numerical simulations (DNS) of particle deposition in wall bounded turbulent flows were performed by McLaughlin (1989) and Ounis et al. (1991, 1993). These studies were concerned with clarifying the particle deposition mechanisms. Brooke et al. (1992) performed detailed DNS studies of vortical structures in the viscous sublayer. Pedinotti et al. (1992) used the DNS to investigate the particle behavior in the wall region of turbulent flows. They reported that an initially uniform distribution of particles tends to segregate into low speed streaks and resuspension occurs by particles being ejected from the wall. The DNS simulation was used by Soltani and Ahmadi (1995) to study the particle entrainment process in a turbulent channel flow. They found that the wall coherent structure plays a dominant role in the particle entrainment process.

Squires and Eaton (1991a) simulated a homogeneous isotropic nondecaying turbulent flow field by imposing an excitation at low wave numbers, and studied the effects of inertia on particle dispersion. They also used the DNS procedure to study the preferential microconcentration structure of particles as a function of Stokes number in turbulent near wall flows (Squires and Eaton, 1991b). Kulick et al. (1994) studied the particle response and turbulence modification in a fully developed turbulent channel flow. Rashidi et al. (1990) performed an experiment to study the particle–turbulence interactions near a wall. They reported that the particle transport is mainly controlled by the turbulence burst phenomena.

The currently available theoretical works on turbulent deposition are exclusively concerned with idealized spherical particles. Most natural dust and solid aerosol particles generated in industrial processes are, however, nonspherical. The motions of nonspherical particles in turbulent flows are much more complicated than those of their spherical counterpart. For nonspherical particles, the orientation and rotational motion are strongly coupled with translation motion and their effects can no longer be neglected.

In the past two decades, transport of nonspherical aerosol particles has received increasing attention. Gallily and co-worker (Gallily and Eisner, 1979; Galliy and Cohen, 1979; Schiby and Gallily, 1980; Einser and Gallily, 1982; Krushkal and Gallily, 1984) conducted a series of theoretical and experimental studies on the orderly, as well as stochastic motions of ellipsoidal particle in laminar flows. Asgharian et al. (1988), Asgharian and Yu (1989), Chen and Yu (1990), and Johnson and Martonen (1993) studied the deposition of fibers in the pulmonary track of humans and animals. Detailed analysis of ellipsoidal particle motion in shear flows was performed by Hinch and Leal (1976), Koch and Shaqfeh (1990), and Shaqfeh and Fredrickson (1990). Massah et al. (1993) studied the motion of fibers in transient rheological flows and in a turbulent flow. Foss et al. (1989) and Schamberger et al. (1990) analyzed the collection process of prolate spheroids by spherical collectors. Gradon et al. (1989) considered the deposition of fibrous particles on a filter element.

Studies of the motions of nonspherical particles in turbulent flows are, however, rather scarce. Recently, Krushkal and Gallily (1988) described the orientation density function of ellipsoidal particles in turbulent shear flows and discussed its application to the atmospheric boundary layer. Fan and Ahmadi (1993, 1995b) studied the dispersion of ellipsoidal particles in an isotropic pseudoturbulent flow field. A procedure involving Euler's four parameters, which avoids the inherent singularity of using Euler angles, was also adopted by Fan and Ahmadi (1995b,c). Recently, Fan et al. (1997), Soltani et al. (1997), and Soltani and Ahmadi (2000) evaluated the hydrodynamic forces and torques acting on multi-link fibers by treating each link as being an elongated ellipsoid. The dispersion of multi-link fibers was then analyzed numerically by Soltani and Ahmadi (2000).

In this work, ellipsoidal particle transport and deposition in dilute turbulent channel flows are studied. The turbulent flow field is generated by the direct numerical simulation of the Navier–Stokes equation. The hydrodynamic drag and torque, the shear-induced lift and gravitational forces are included in the governing equations. Euler's four parameters (also known as quaternions) are used for describing the time evolution of ellipsoidal orientation. The predicted deposition velocities are compared with the available experimental data and the earlier simulation results. Ensembles of ellipsoidal particle trajectories are evaluated and statistically analyzed. The effects of particle size, aspect ratio, turbulence near wall eddies, and various forces acting on the particles are studied. The deposition rates of ellipsoidal particles are also evaluated and the results are compared with the available experimental data.

2. Assumptions and limitations

To make the simulation of fiber transport in turbulent flow manageable, several assumptions were made. It is assumed that the flow is sufficiently dilute that the effect of particles on the flow can be neglected. In addition, the particle–particle collision as well as aggregation effects are ignored. The fiber diameters used are also greater than 1 μm, with an aspect ratio between 1 and 10. Thus, the Brownian motion of these particles is also negligible. Another important assumption made is that the fiber size is, generally, less than the Kolmogorov length-scale. Since the slip velocity is small, the expressions for the forces and torques acting on the fiber under the creeping flow regime can be used.

Therefore, the simulation results are limited to dilute flows, and for collection of fibers that are larger than a few micrometers, but smaller than the turbulence Kolmogorov length-scale. While these limitations are quite important, the simulation results are applicable for dilute air flows with a velocity of a few m/s in ducts with a diameter of a few centimeters, which have many practical applications.

3. Turbulent flow velocity field

The instantaneous fluid velocity field in the channel is evaluated by the DNS of the Navier–Stokes equation. It is assumed that the fluid is incompressible and a constant mean pressure gradient in the x-direction is imposed. The corresponding governing equations of motion are:

$$\nabla \cdot \mathbf{u} = 0, \tag{1}$$

$$\frac{\partial \mathbf{u}}{\partial t} + \mathbf{u} \cdot \nabla \mathbf{u} = \nu \nabla^2 \mathbf{u} - \frac{1}{\rho^{\mathrm{f}}} \nabla P, \tag{2}$$

where $\mathbf{u}$ is the fluid velocity vector, P the pressure, ρ^{f} the density, and ν is the kinematic viscosity. The fluid velocity is assumed to satisfy the no slip boundary conditions at the channel walls. In wall units, the channel has a width of 250, and a 630×630 periodic segment in the x- and z-directions is used in the simulations. A $16 \times 65 \times 64$ computational grid in the x-, y-, z-directions is also employed. The grid spacings in the x- and z-directions are constant, while the variation of grid points in the y-direction is represented by the Chebyshev series. The distance of the ith grid point in the y-direction from the centerline is given as

$$y_i = \frac{h}{2} \cos(\pi i / M), \quad 0 \leqslant i \leqslant M. \tag{3}$$

Here $M = 64$ and there are 65 grid points in the y-direction.

The channel flow code used in this study is the one developed by McLaughlin (1989). To solve for the velocity components by pseudospectral methods, the fluid velocity is expanded in a three-dimensional Fourier–Chebyshev series. The fluid velocity field in the x- and z-directions is expanded by the Fourier series, while in the y-direction the Chebyshev series is used. The code uses an Adams–Bashforth–Crank–Nickolson (ABCN) scheme to compute the nonlinear and viscous terms in the Navier–Stokes equation and performs three fractional time steps to forward the fluid velocity from time step (N) to time step $(N + 1)$. The details of the numerical techniques were described by McLaughlin (1989). In these computer simulations, wall units are used and all variables are nondimensionalized in terms of the shear velocity u^* and kinematic viscosity ν.

McLaughlin (1989) showed that the near wall root-mean-square (RMS) fluctuation velocities as predicted by the present DNS code are in good agreement with the high resolution DNS code of Kim et al. (1987). Zhang and Ahmadi (2000) showed that the present DNS with a grid size of $16 \times 64 \times 64$ can produce first- and second-order turbulence statistics that are reasonably accurate when compared with the results of high resolution grids of $32 \times 64 \times 64$ and $32 \times 128 \times 128$. In this study, for the sake of computational economy, the coarser grid is used.

Fig. 1 shows a sample instantaneous velocity field at $t^+ = 100$ in different planes. While the velocity field in the y–z plane (at $x^+ = 157.5$) shown in Fig. 1(a) has a random pattern, near wall coherent eddies and flow streams towards and away from the wall can be observed from this figure. Fig. 1(b) shows the velocity vector plot in the x–y plane (at $z^+ = 157.5$). Random deviations from the expected mean velocity profile are clearly seen. The velocity field in the x–z plane (at $y^+ = 88.4$) shown in Fig. 1(c) indicates that the flow is predominantly in the x-direction. The near wall low and high speed streaks are also noticeable from this figure.

4. Ellipsoidal particle equation of motion

This section outlines the kinematics and dynamics of a rigid nonspherical particle suspended in the turbulent channel flow field.

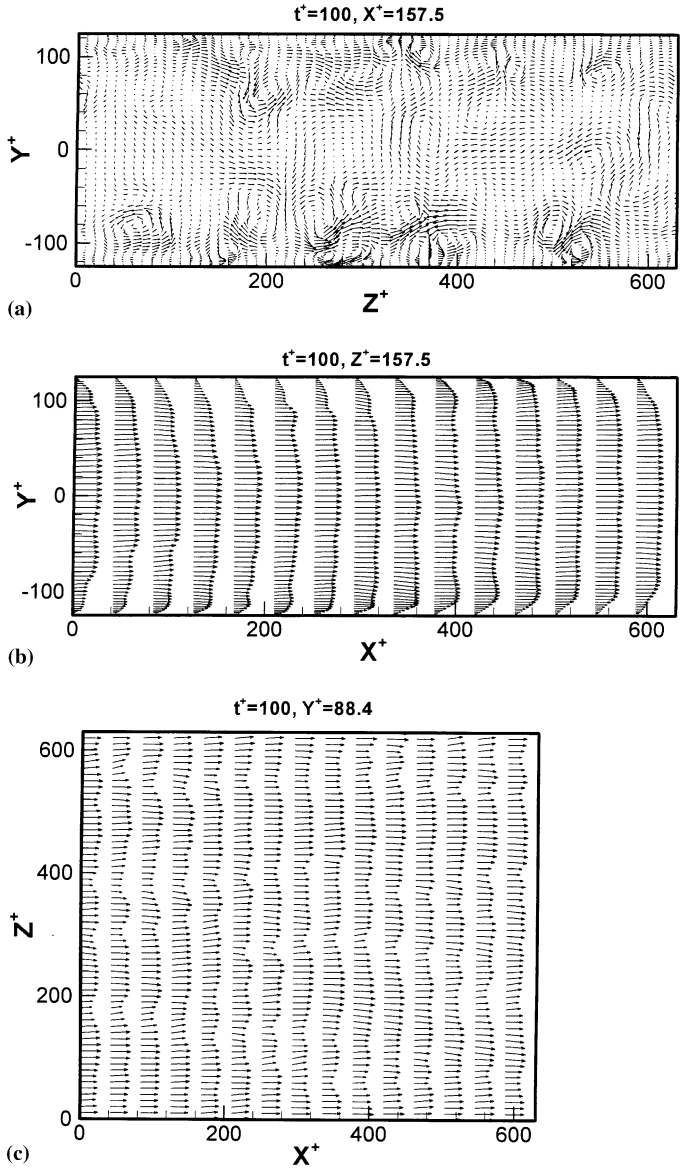

Fig. 1. Sample velocity plot parallel to (a) the y–z plane, (b) the x–y plane, (c) the x–z plane.

4.1. Kinematics

Fig. 2(a) shows the coordinate systems associated with the motion of an ellipsoidal particle in a general flow field. Here, $\mathbf{x} = [x, y, z]$ is the inertial coordinates, and $\hat{\mathbf{x}} = [\hat{x}, \hat{y}, \hat{z}]$ is the particle coordinate system with its origin being at the particle mass center and its axes being the principal axis. In this figure, a third coordinate system $\hat{\hat{\mathbf{x}}} = [\hat{\hat{x}}, \hat{\hat{y}}, \hat{\hat{z}}]$ with its origin coinciding with that of the particle frame and its axes being parallel to the corresponding axes of the inertial frame is also

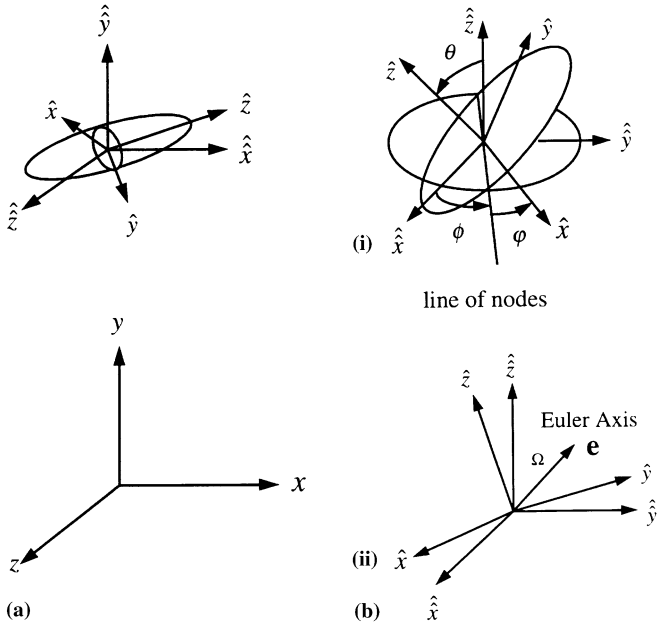

Fig. 2. (a) An ellipsoidal particle and the corresponding coordinate systems; (b) coordinate systems defining (i) the Euler angles and (ii) Euler's four parameters.

shown. This third coordinate system will be referred to as the co-moving frame. The transformation between the co-moving frame coordinates and the particle frame coordinates is given by the linear relation

$$\hat{\mathbf{x}} = \mathbf{A}\hat{\hat{\mathbf{x}}}. \tag{4}$$

Here, a boldfaced capital letter denotes a matrix while a boldfaced lower-case letter denotes a vector. According to Goldstein (1980) and Hughes (1986), the transformation matrix $\mathbf{A} = [a_{ij}]$ may be expressed in terms of Euler angles or Euler's four parameters (quaternions) i.e.,

$$\mathbf{A} = \begin{bmatrix} \cos\psi\cos\phi - \cos\theta\sin\phi\sin\psi & \cos\psi\sin\phi + \cos\theta\cos\phi\sin\psi & \sin\psi\sin\theta \\ -\sin\psi\cos\phi - \cos\theta\sin\phi\cos\psi & -\sin\psi\sin\phi + \cos\theta\cos\phi\cos\psi & \cos\psi\sin\theta \\ \sin\theta\sin\phi & -\sin\theta\cos\phi & \cos\theta \end{bmatrix} \tag{5}$$

or

$$\mathbf{A} = \begin{bmatrix} 1-2(\varepsilon_2^2+\varepsilon_3^2) & 2(\varepsilon_1\varepsilon_2+\varepsilon_3\eta) & 2(\varepsilon_1\varepsilon_3-\varepsilon_2\eta) \\ 2(\varepsilon_2\varepsilon_1-\varepsilon_3\eta) & 1-2(\varepsilon_3^2+\varepsilon_1^2) & 2(\varepsilon_2\varepsilon_3+\varepsilon_1\eta) \\ 2(\varepsilon_3\varepsilon_1+\varepsilon_2\eta) & 2(\varepsilon_3\varepsilon_2-\varepsilon_1\eta) & 1-2(\varepsilon_1^2+\varepsilon_2^2) \end{bmatrix}, \tag{6}$$

where ϕ, θ, and ψ are the Euler angles (the x-convention of Goldstein, 1980), while ε_1, ε_2, ε_3, η are Euler's four parameters. Fig. 2(b)(i) and (ii) illustrates the definition of the Euler angles and Euler's four parameters. The Euler four parameters are related to the axis and angle of rotation by $[\varepsilon_1, \varepsilon_2, \varepsilon_3]^{\mathrm{T}} = \mathbf{e}\sin(\Omega/2)$ and $\eta = \cos(\Omega/2)$, where superscript T denotes a transpose, $\mathbf{e}$ the unit vector along the axis of rotation, and Ω is the angle of rotation. In this study, due to the inevitable

singularity in evaluating the time rates of changes of Euler angles (Fan and Ahmadi, 1995b,c), Eq. (6) is used in the numerical simulation of particle motions. However, Euler angles which are mutually independent variables and Eq. (5) are used to assign the initial particle orientations.

The most general rotation of a rigid body has three degrees of freedom. Therefore, Euler's four parameters are subject to a constraint given as

$$\varepsilon_1^2 + \varepsilon_2^2 + \varepsilon_3^3 + \eta^2 = 1. \tag{7}$$

The four parameters may also be expressed in terms of the elements of the transformation matrix or the Euler angles. That is, for $\eta \neq 0$,

$$\eta = \pm\tfrac{1}{2}(1 + a_{11} + a_{22} + a_{33})^{1/2} = \pm\tfrac{1}{2}[(1 + \cos\theta)(1 + \cos(\phi + \psi))]^{1/2}, \tag{8}$$

$$\begin{bmatrix} \varepsilon_1 \\ \varepsilon_2 \\ \varepsilon_3 \end{bmatrix} = \frac{1}{4\eta}\begin{bmatrix} a_{23} - a_{32} \\ a_{31} - a_{13} \\ a_{12} - a_{21} \end{bmatrix} = \frac{1}{4\eta}\begin{bmatrix} \sin\theta(\cos\phi + \cos\psi) \\ \sin\theta(\sin\phi - \sin\psi) \\ (1 + \cos\theta)\sin(\phi + \psi) \end{bmatrix}. \tag{9}$$

For $\eta = 0$,

$$\varepsilon_1 = \pm\sqrt{\frac{1 + a_{11}}{2}}, \tag{10}$$

$$\varepsilon_2 = \frac{a_{12}}{2\varepsilon_1}, \tag{11}$$

$$\varepsilon_3 = \frac{a_{23}}{2\varepsilon_2}, \tag{12}$$

where a_{ij} (elements of **A**) are the direction cosines. The nonuniqueness of the values as given by Eqs. (8)–(12) does not introduce any difficulty because both the choices lead to the same particle trajectory.

The time rates of change of $[\varepsilon_1, \varepsilon_2, \varepsilon_3, \eta]$ are related to the particle angular velocities with respect to the particle frame, $[\omega_{\hat{x}}, \omega_{\hat{y}}, \omega_{\hat{z}}]$ i.e.,

$$\begin{bmatrix} \mathrm{d}\varepsilon_1/\mathrm{d}t \\ \mathrm{d}\varepsilon_2/\mathrm{d}t \\ \mathrm{d}\varepsilon_3/\mathrm{d}t \\ \mathrm{d}\eta/\mathrm{d}t \end{bmatrix} = \frac{1}{2}\begin{bmatrix} \eta\omega_{\hat{x}} - \varepsilon_3\omega_{\hat{y}} + \varepsilon_2\omega_{\hat{z}} \\ \varepsilon_3\omega_{\hat{x}} + \eta\omega_{\hat{y}} - \varepsilon_1\omega_{\hat{z}} \\ -\varepsilon_2\omega_{\hat{x}} + \varepsilon_1\omega_{\hat{y}} + \eta\omega_{\hat{z}} \\ -\varepsilon_1\omega_{\hat{x}} - \varepsilon_2\omega_{\hat{y}} - \varepsilon_3\omega_{\hat{z}} \end{bmatrix}, \tag{13}$$

where t is the time.

The translational displacement of the particle is described by

$$\frac{\mathrm{d}\mathbf{x}}{\mathrm{d}t} = \mathbf{v}, \tag{14}$$

where **v** is the translational velocity vector of the particle mass center.

4.2. Dynamics

For a nonspherical particle moving in a general flow field, the translational motion in the laboratory frame and the rotational motion in the particle frame are governed by

$$m^{\mathrm{p}}\frac{\mathrm{d}\mathbf{v}}{\mathrm{d}t} = \left(m^{\mathrm{p}} - m^{\mathrm{f}}\right)\mathbf{g} + \mathbf{f}^{\mathrm{h}} + \mathbf{f}^{\mathrm{L}}, \tag{15}$$

$$I_{\hat{x}}\frac{\mathrm{d}\omega_{\hat{x}}}{\mathrm{d}t} - \omega_{\hat{y}}\omega_{\hat{z}}\left(I_{\hat{y}} - I_{\hat{z}}\right) = T^{\mathrm{h}}_{\hat{x}}, \tag{16}$$

$$I_{\hat{y}}\frac{\mathrm{d}\omega_{\hat{y}}}{\mathrm{d}t} - \omega_{\hat{z}}\omega_{\hat{x}}\left(I_{\hat{z}} - I_{\hat{x}}\right) = T^{\mathrm{h}}_{\hat{y}}, \tag{17}$$

$$I_{\hat{z}}\frac{\mathrm{d}\omega_{\hat{z}}}{\mathrm{d}t} - \omega_{\hat{x}}\omega_{\hat{y}}\left(I_{\hat{x}} - I_{\hat{y}}\right) = T^{\mathrm{h}}_{\hat{z}}. \tag{18}$$

In these equations, the following notations are used:

m^{p}	mass of the particle
m^{f}	mass of the fluid the particle displaces
t	time
$\mathbf{v} = [v_x, v_y, v_z]$	translational velocity vector of the particle mass center
$\mathbf{g} = [g_x, g_y, g_z]$	acceleration of gravity
$\mathbf{f}^{\mathrm{h}} = \left[f^{\mathrm{h}}_x, f^{\mathrm{h}}_y, f^{\mathrm{h}}_z\right]$	hydrodynamic drag acting on the particle
$\mathbf{f}^{\mathrm{L}} = \left[f^{\mathrm{L}}_x, f^{\mathrm{L}}_y, f^{\mathrm{L}}_z\right]$	shear-induced lift acting on the particle
$I_{\hat{x}}, I_{\hat{y}}, I_{\hat{z}}$	particle moments of inertia about the principal axes $(\hat{x}, \hat{y}, \hat{z})$
$\omega_{\hat{x}}, \omega_{\hat{y}}, \omega_{\hat{z}}$	particle angular velocities with respect to the principal axes
$T^{\mathrm{h}}_{\hat{x}}, T^{\mathrm{h}}_{\hat{y}}, T^{\mathrm{h}}_{\hat{z}}$	hydrodynamic torque acting on the particle with respect to the principal axes

It should be emphasized that, in Eqs. (15)–(18), the translation motion is expressed in the inertial frame, while the rotational motion is stated in the particle frame.

4.3. Hydrodynamic drag

The hydrodynamic drag force acting on an ellipsoidal particle in a general flow field under Stokes flow condition was obtained by Brenner (1964) in the form of an infinite series of fluid velocity and its spatial derivatives. The higher-order terms are proportional to higher-order powers of particle minor axis. Retaining only the first term of the series for small particles, it follows that

$$\mathbf{f}^{\mathrm{h}} = \mu\pi a\hat{\hat{\mathbf{K}}}\cdot(\mathbf{u} - \mathbf{v}), \tag{19}$$

where μ is the dynamic viscosity of the fluid, a is the semi-minor axis of the ellipsoid of revolution and $\mathbf{u} = [u_x, u_y, u_z]$ is the fluid velocity vector at the particle centroid in the absence of the particle. In this equation, the translation dyadic (also known as the resistance tensor) is given by

$$\hat{\hat{\mathbf{K}}} = \mathbf{A}^{-1}\hat{\mathbf{K}}\mathbf{A}. \tag{20}$$

The particle–frame translation dyadic $\hat{\mathbf{K}} = [k_{ij}]$ for an ellipsoid of revolution along the $\hat{z}$-axis is a diagonal matrix with

$$k_{\hat{x}\hat{x}} = k_{\hat{y}\hat{y}} = \frac{16(\beta^2-1)}{\left[(2\beta^2-3)\ln\left(\beta+\sqrt{\beta^2-1}\right)/\sqrt{\beta^2-1}\right]+\beta}, \tag{21}$$

$$k_{\hat{z}\hat{z}} = \frac{8(\beta^2-1)}{\left[(2\beta^2-1)\ln\left(\beta+\sqrt{\beta^2-1}\right)/\sqrt{\beta^2-1}\right]-\beta}, \tag{22}$$

where $\beta = b/a$ is the particle aspect ratio (ratio of the semi-major axis to the semi-minor axis). Note also that the elements of the particle–frame translation dyadic are such that the translation dyadics, $\hat{\mathbf{K}}$ and $\hat{\hat{\mathbf{K}}}$, are dimensionless quantities (Fan and Ahmadi, 1995c).

4.4. Shear-induced lift

The shear-induced lift force acting on an arbitrary-shaped particle was obtained by Harper and Chang (1968) as

$$\mathbf{f}^{\mathrm{L}} = \frac{\pi^2\mu a^2}{\nu^{1/2}}\frac{\partial u_x/\partial y}{|\partial u_x/\partial y|^{1/2}}\left(\hat{\hat{\mathbf{K}}}\cdot\mathbf{L}\cdot\hat{\hat{\mathbf{K}}}\right)\cdot(\mathbf{u}-\mathbf{v}), \tag{23}$$

where

$$\mathbf{L} = \begin{bmatrix} 0.0501 & 0.0329 & 0.00 \\ 0.0182 & 0.0173 & 0.00 \\ 0.00 & 0.00 & 0.0373 \end{bmatrix}. \tag{24}$$

For the limiting case of a spherical particle, Eq. (23) reduces to

$$\mathbf{f}^{\mathrm{L}} = \frac{36\pi^2\mu a^2}{\nu^{1/2}}\frac{\partial u_x/\partial y}{|\partial u_x/\partial y|^{1/2}}\mathbf{L}\cdot(\mathbf{u}-\mathbf{v}). \tag{25}$$

Note that the y-component lift force induced by the velocity difference in the x-direction as evaluated from Eq. (25) agrees with the result of Saffman (1965, 1968). Recently Cherukat and McLaughlin (1990), McLaughlin (1991, 1993) provided improved expressions for the lift force acting on spheres by including the wall effects and relaxed certain Reynolds number constraints. However, such corrections for the inertial lift for ellipsoids have not been developed as yet. Earlier simulations reported by Chen and Ahmadi (1997) and McLaughlin (1989) for spherical particles showed that the lift force correction on the particle transport and deposition is small in most situations. Therefore, here Eq. (23) is used.

4.5. Hydrodynamic torque

The hydrodynamic torque acting on an ellipsoidal particle suspended in a linear shear flow was obtained by Jeffery (1922). The flow near a small particle may locally be approximated as a linear shear. Consequently, the result of Jeffery (1922) may be used.

For an ellipsoid of revolution with its major axis along the $\hat{z}$-axis, the expressions for hydrodynamic torques are given as

$$T_{\hat{x}}^{\mathrm{h}} = \frac{16\pi\mu a^3\beta}{3(\beta_0+\beta^2\gamma_0)}\left[(1-\beta^2)d_{\hat{z}\hat{y}} + (1+\beta^2)(w_{\hat{z}\hat{y}}-\omega_{\hat{x}})\right], \tag{26}$$

$$T_{\hat{y}}^{\mathrm{h}} = \frac{16\pi\mu a^3\beta}{3(\alpha_0+\beta^2\gamma_0)}\left[(\beta^2-1)d_{\hat{x}\hat{z}} + (1+\beta^2)(w_{\hat{x}\hat{z}}-\omega_{\hat{y}})\right], \tag{27}$$

$$T_{\hat{z}}^{\mathrm{h}} = \frac{32\pi\mu a^3\beta}{3(\alpha_0+\beta_0)}(w_{\hat{y}\hat{x}}-\omega_{\hat{z}}), \tag{28}$$

where

$$d_{\hat{z}\hat{y}} = \frac{1}{2}\left(\frac{\partial u_{\hat{z}}}{\partial\hat{y}} + \frac{\partial u_{\hat{y}}}{\partial\hat{z}}\right), \quad d_{\hat{x}\hat{z}} = \frac{1}{2}\left(\frac{\partial u_{\hat{x}}}{\partial\hat{z}} + \frac{\partial u_{\hat{z}}}{\partial\hat{x}}\right), \tag{29}$$

$$w_{\hat{z}\hat{y}} = \frac{1}{2}\left(\frac{\partial u_{\hat{z}}}{\partial\hat{y}} - \frac{\partial u_{\hat{y}}}{\partial\hat{z}}\right), \quad w_{\hat{x}\hat{z}} = \frac{1}{2}\left(\frac{\partial u_{\hat{x}}}{\partial\hat{z}} - \frac{\partial u_{\hat{z}}}{\partial\hat{x}}\right), \quad w_{\hat{y}\hat{x}} = \frac{1}{2}\left(\frac{\partial u_{\hat{y}}}{\partial\hat{x}} - \frac{\partial u_{\hat{x}}}{\partial\hat{y}}\right) \tag{30}$$

are the elements of the deformation rate and the spin tensors. The dimensionless parameters in Eqs. (26)–(28) were given by Galliy and Cohen (1979) as

$$\alpha_0 = \beta_0 = \frac{\beta^2}{\beta^2-1} + \frac{\beta}{2(\beta^2-1)^{3/2}}\ln\left[\frac{\beta-\sqrt{\beta^2-1}}{\beta+\sqrt{\beta^2-1}}\right], \tag{31}$$

$$\gamma_0 = -\frac{2}{\beta^2-1} - \frac{\beta}{(\beta^2-1)^{3/2}}\ln\left[\frac{\beta-\sqrt{\beta^2-1}}{\beta+\sqrt{\beta^2-1}}\right]. \tag{32}$$

The velocity gradient in the particle frame needed in Eqs. (29) and (30) may be obtained using the transformation

$$\hat{\mathbf{G}} = \mathbf{A}\hat{\tilde{\mathbf{G}}}\mathbf{A}^{-1}, \tag{33}$$

where $\hat{\mathbf{G}}$ and $\hat{\tilde{\mathbf{G}}}$ stand for dyadics expressed in the particle and the co-moving frames, respectively.

4.6. Nondimensional equation of motion

In Eqs. (15)–(18) the mass of the ellipsoid of revolution and the displaced fluid mass are given as

$$m^{\mathrm{p}} = \frac{4}{3}\pi a^3\beta\rho^{\mathrm{p}}, \quad m^{\mathrm{f}} = \frac{4}{3}\pi a^3\beta\rho^{\mathrm{f}}, \tag{34}$$

where ρ^{p} and ρ^{f} denote the densities of the particle and the fluid, respectively. The principal moments of inertia for the particle are given by

$$I_{\hat{x}} = I_{\hat{y}} = \frac{(1+\beta^2)a^2}{5} m^{\mathrm{p}}, \quad I_{\hat{z}} = \frac{2a^2}{5} m^{\mathrm{p}}. \tag{35}$$

The nondimensional governing equations may be obtained using the following dimensionless quantities (wall units)

$$\mathbf{u}^+ = \frac{\mathbf{u}}{u^*}, \quad \mathbf{v}^+ = \frac{\mathbf{v}}{u^*}, \quad \mathbf{x}^+ = \frac{\mathbf{x}}{u^*}, \quad a^+ = \frac{au^*}{\nu}, \quad t^+ = \frac{tu^{*2}}{\nu}, \tag{36}$$

$$\omega_{\hat{x}}^+ = \frac{\omega_{\hat{x}}\nu}{u^{*2}}, \quad \omega_{\hat{y}}^+ = \frac{\omega_{\hat{y}}\nu}{u^{*2}}, \quad \omega_{\hat{z}}^+ = \frac{\omega_{\hat{z}}\nu}{u^{*2}}. \tag{37}$$

Using Eqs. (19) and (23), Eqs. (13)–(18) may be restated in nondimensional forms as

$$\frac{\mathrm{d}\mathbf{x}^+}{\mathrm{d}t^+} = \mathbf{v}^+, \tag{38}$$

$$\begin{bmatrix} \mathrm{d}\varepsilon_1/\mathrm{d}t^+ \\ \mathrm{d}\varepsilon_2/\mathrm{d}t^+ \\ \mathrm{d}\varepsilon_3/\mathrm{d}t^+ \\ \mathrm{d}\eta/\mathrm{d}t^+ \end{bmatrix} = \frac{1}{2} \begin{bmatrix} \eta\omega_{\hat{x}}^+ - \varepsilon_3\omega_{\hat{y}}^+ + \varepsilon_2\omega_{\hat{z}}^+ \\ \varepsilon_3\omega_{\hat{x}}^+ + \eta\omega_{\hat{y}}^+ - \varepsilon_1\omega_{\hat{z}}^+ \\ -\varepsilon_2\omega_{\hat{x}}^+ + \varepsilon_1\omega_{\hat{y}}^+ + \eta\omega_{\hat{z}}^+ \\ -\varepsilon_1\omega_{\hat{x}}^+ - \varepsilon_2\omega_{\hat{y}}^+ - \varepsilon_3\omega_{\hat{z}}^+ \end{bmatrix}, \tag{39}$$

$$\begin{aligned} \frac{\mathrm{d}\mathbf{v}^+}{\mathrm{d}t^+} = {} & \left(\frac{S-1}{S}\right)\mathbf{g}^+ + \frac{3}{4\beta Sa^{+2}}\hat{\hat{\mathbf{K}}}\cdot(\mathbf{u}^+ - \mathbf{v}^+) \\ & + \frac{3\pi}{4\beta Sa^+} \frac{\partial u_x^+/\partial y^+}{\left|\partial u_x^+/\partial y^+\right|^{1/2}} \left(\hat{\hat{\mathbf{K}}}\cdot\mathbf{L}\cdot\hat{\hat{\mathbf{K}}}\right)\cdot(\mathbf{u}^+ - \mathbf{v}^+), \end{aligned} \tag{40}$$

$$\begin{aligned} \frac{\mathrm{d}\omega_{\hat{x}}^+}{\mathrm{d}t^+} = {} & \omega_{\hat{y}}^+\omega_{\hat{z}}^+\left(1 - \frac{2}{1+\beta^2}\right) + \frac{20}{(\beta_0 + \beta^2\gamma_0)(1+\beta^2)Sa^{+2}} \\ & \times \left[(1-\beta^2)d_{\hat{z}\hat{y}}^+ + (1+\beta^2)\left(w_{\hat{z}\hat{y}}^+ - \omega_{\hat{x}}^+\right)\right], \end{aligned} \tag{41}$$

$$\begin{aligned} \frac{\mathrm{d}\omega_{\hat{y}}^+}{\mathrm{d}t^+} = {} & \omega_{\hat{z}}^+\omega_{\hat{x}}^+\left(\frac{2}{1+\beta^2} - 1\right) + \frac{20}{(\alpha_0 + \beta^2\gamma_0)(1+\beta^2)Sa^{+2}} \\ & \times \left[(\beta^2-1)d_{\hat{x}\hat{z}}^+ + (1+\beta^2)\left(w_{\hat{x}\hat{z}}^+ - \omega_{\hat{y}}^+\right)\right], \end{aligned} \tag{42}$$

$$\frac{\mathrm{d}\omega_{\hat{z}}^+}{\mathrm{d}t^+} = \frac{20}{(\alpha_0 + \beta_0)Sa^{+2}}\left(w_{\hat{y}\hat{x}}^+ - \omega_{\hat{z}}^+\right). \tag{43}$$

In Eq. (40), the density ratio and the nondimensional gravitational acceleration are defined as

$$S = \frac{\rho^{\mathrm{p}}}{\rho^{\mathrm{f}}}, \quad \mathbf{g}^+ = \frac{\nu}{u^{*3}}\mathbf{g} \tag{44}$$

are also used. Here superscript "+" identifies a nondimensionalized quantity. Therefore,

$$d^+_{\hat{z}\hat{y}} = \frac{1}{2}\left(\frac{\partial u^+_{\hat{z}}}{\partial \hat{y}^+} + \frac{\partial u^+_{\hat{y}}}{\partial \hat{z}^+}\right), \quad d^+_{\hat{z}\hat{x}} = \frac{1}{2}\left(\frac{\partial u^+_{\hat{x}}}{\partial \hat{z}^+} + \frac{\partial u^+_{\hat{z}}}{\partial \hat{x}^+}\right), \tag{45}$$

$$w^+_{\hat{z}\hat{y}} = \frac{1}{2}\left(\frac{\partial u^+_{\hat{z}}}{\partial \hat{y}^+} - \frac{\partial u^+_{\hat{y}}}{\partial \hat{z}^+}\right), \quad w^+_{\hat{x}\hat{z}} = \frac{1}{2}\left(\frac{\partial u^+_{\hat{x}}}{\partial \hat{z}^+} - \frac{\partial u^+_{\hat{z}}}{\partial \hat{x}^+}\right), \quad w^+_{\hat{z}\hat{y}} = \frac{1}{2}\left(\frac{\partial u^+_{\hat{y}}}{\partial \hat{x}^+} - \frac{\partial u^+_{\hat{x}}}{\partial \hat{y}^+}\right) \tag{46}$$

are, respectively, the nondimensional deformation rate and spin tensors. When the nondimensional parameters for physical properties of the ellipsoidal particles and the flow field are specified, Eqs. (38)–(43) may be used to evaluate the particle translational and rotational motions.It is advantageous to introduce a suitable equivalent relaxation time for the ellipsoidal particles. Shapiro and Goldenberg (1993) suggested using a relaxation time based on the assumption of isotropic particle orientation and the averaged mobility dyadic (inverse of the translation dyadic), i.e.,

$$\tau^+_{\mathrm{eq}} = \frac{4\beta Sa^{+2}}{9}\left(\frac{1}{k_{\hat{x}\hat{x}}} + \frac{1}{k_{\hat{y}\hat{y}}} + \frac{1}{k_{\hat{z}\hat{z}}}\right) = \frac{2\beta Sa^{+2}}{9}\frac{\ln\left(\beta + \sqrt{\beta^2 - 1}\right)}{\sqrt{\beta^2 - 1}}. \tag{47}$$

Fan and Ahmadi (1995b) used the orientation averaged translation dyadic instead of the mobility dyadic. Accordingly, the equivalent particle relaxation time is defined as

$$\tau^+_{\mathrm{eq}} = \frac{4\beta Sa^{+2}}{k_{\hat{x}\hat{x}} + k_{\hat{y}\hat{y}} + k_{\hat{z}\hat{z}}}. \tag{48}$$

It should be emphasized that both Eqs. (47) and (48) reduce to the correct $\tau^+_p = 2Sa^{+2}/9$ at the limit of spherical particles. It was also shown by Fan and Ahmadi (1995b) that both definitions for equivalent relaxation time serve equally well in characterizing the motion of ellipsoidal particles. Eq. (48) is used in the subsequent sections for evaluating the equivalent relaxation time of ellipsoidal particles.

5. Deposition velocity and empirical model

The dimensionless deposition velocity for particles with a uniform concentration C_0 near a surface is defined as

$$u^+_{\mathrm{d}} = J/(C_0 u^*), \tag{49}$$

where J is the particle mass flux to the wall per unit time. In the computer simulation, the particle deposition velocity is estimated as

$$u^+_{\mathrm{d}} = \frac{N_{\mathrm{d}}/t^+_{\mathrm{d}}}{N_0/y^+_0}, \tag{50}$$

where N_0 is the initial number of particles uniformly distributed in a region within a distance of y^+_0 from the wall, and N_{d} is the number of deposited particles in the time duration t^+_{d}. In practice, the time duration should be selected in the quasi-equilibrium condition when $N_{\mathrm{d}}/t^+_{\mathrm{d}}$ becomes a constant.

Shapiro and Goldenberg (1993) proposed several empirical equations for predicting the effect of fiber length on the deposition velocity in vertical and horizontal ducts. Kvasnak and Ahmadi (1995) modified Wood's equation along the lines of Shapiro and Goldenberg to obtain an improved empirical model for the deposition velocity of straight fibers given as

$$u_{\mathrm{d}}^{+} = 4.5 \times 10^{-4}\tau_{\mathrm{eq}}^{+2} + 5 \times 10^{-3}L^{+2} + \tau_{\mathrm{eq}}^{+}g^{+}, \tag{51}$$

where $L^{+} = Lu^{*}/\nu = 2a^{+}\beta$ is the nondimensional particle length. The first term in Eq. (51) is the ellipsoidal particle deposition induced by eddy diffusion impaction. The second term is due to the interception mechanism and the third term corresponds to the gravitational sedimentation in horizontal ducts.

Fan and Ahmadi (1993) developed a semi-empirical equation for the deposition velocity of spherical particles on smooth and rough surfaces in vertical ducts. Fan and Ahmadi (2000) extended their equation to cover Brownian diffusion of straight fibers in turbulent flows. Soltani and Ahmadi (2000) also provided a modified equation for application to curly fiber deposition on smooth surfaces in the absence of gravitational effects and lift force.

Based on the expression for τ_{eq}^{+} given by Eq. (48), an equivalent particle diameter may be defined, i.e.,

$$d_{\mathrm{eq}}^{+} = \sqrt{\frac{18\tau_{\mathrm{eq}}^{+}}{S}}. \tag{52}$$

When gravitational effects are present, the following empirical equation for ellipsoidal particle deposition on smooth surface is proposed:

$$u_{\mathrm{d}}^{+} = \begin{cases} 0.0185 \times \left[\dfrac{\frac{\beta L^{+2}}{\beta+3} + \frac{4\beta\tau_{\mathrm{eq}}^{+2}g^{+}L_1^{+}}{0.01085(\beta+3)(1+\tau_{\mathrm{eq}}^{+2}L_1^{+})}}{3.42 + \frac{\tau_{\mathrm{eq}}^{+2}g^{+}L_1^{+}}{0.01085(1+\tau_p^{+2}L_1^{+})}}\right] & \text{if} \quad u_{\mathrm{d}}^{+} < 0.14, \\ \times\left[1 + 8\mathrm{e}^{-(\tau_{\mathrm{eq}}^{+}-10)^2/32}\right]\dfrac{1}{1-\tau_{\mathrm{eq}}^{+2}L_1^{+}(1+(g^{+}/0.037))} & \\ 0.14 & \text{otherwise}, \end{cases} \tag{53}$$

where the nondimensional lift coefficient is defined as

$$L_1^{+} = \frac{3.08}{Sd_{\mathrm{eq}}^{+}} = \frac{0.725}{\sqrt{S\tau_{\mathrm{eq}}^{+}}}. \tag{54}$$

For $\beta = 1$, Eq. (53) reduces to the empirical equation for spherical particles suggested by Fan and Ahmadi (1993). In Eq. (53), g^{+} is the nondimensional acceleration of gravity given by Eq. (44). For downward duct flows, g^{+} is positive and for upward flows, g^{+} is negative. For a horizontal channel, $g^{+} = 0$ and the gravitational sedimentation velocity $\tau_{\mathrm{eq}}^{+}g^{+}$ should be added to Eq. (53). This equation is used in the next section for comparison with the DNS results and the experimental data for elongated particle deposition rates.

6. Simulation procedure

A computer program for solving the translation and rotation of an ellipsoidal particle in the three-dimensional turbulent flow fields generated by the DNS is developed. The computational algorithm consists of the following steps:

1. Initial positions and orientations (Euler's angles ϕ, θ and ψ) of ellipsoids and the initial velocity conditions for particle velocities and angular velocities are specified. Here the fiber initial velocities and angular velocities are set equal to that of fluid velocities and angular velocities at the ellipsoid centroids.
2. Parameters $\varepsilon_1, \varepsilon_2, \varepsilon_3$, and η are evaluated using Eqs. (8)–(12).
3. Eqs. (5) and (6) are used to obtain the transformation matrix $\mathbf{A}$.
4. The fluid velocity, $\mathbf{u}^+$, and the fluid velocity gradient tensor, $\partial u_k^+/\partial x_l^+$, at each particle centroid are evaluated and Eqs. (20) and (33) are used to obtain the resistance and velocity gradient matrices $\hat{\mathbf{K}}$ and $\hat{\mathbf{G}}$.
5. Equations of motion as given by Eqs. (38)–(43) are solved for determining the new particle position and Euler's parameters.
6. The program returns to step 3 and continues the procedure until the desired time period or the termination condition is reached.

The fourth-order Runge–Kutta scheme is used for the numerical integration of Eq. (39) and the Adams scheme is used to advance the particle positions. The implicit Euler backward scheme is used to discretize Eqs. (40)–(43) to obtain the new velocity and angular velocity of each ellipsoid. Here, $\Delta t^+ = 0.2$ (i.e., $\Delta t = 3.33 \times 10^{-5}$ s for $u^* = 0.3$ m/s and $\nu = 1.5 \times 10^{-5}\mathrm{m}^2/\mathrm{s}$) is used for integrating the equations of motion.

7. Simulation results

In this section, results concerning transport and deposition of ellipsoidal particles in turbulent channel flows are presented. In the simulation, a temperature of $T = 298$ K, a kinematic viscosity of $\nu = 1.5 \times 10^{-5}$ m^2/s, and a density of $\rho^{\mathrm{f}} = 1.12$ kg/m^3 for air are assumed. In such a condition, the flow Reynolds number based on the shear velocity, u^*, and half-channel width is 125, while the flow Reynolds number based on hydraulic diameter and the centerline velocity is about 8000. The density ratio and shear velocity are varied and a range of diameters and aspect ratios are studied. Ensembles of 8192 or 15,000 are used for evaluating the particle trajectories statistics and deposition velocities.

It is assumed that an ellipsoidal particle deposits on a wall when the particle surface touches the wall. The detailed procedure for checking the condition for the ellipsoid to touch the wall was described by Fan and Ahmadi (1995c) and, therefore, is not repeated here.

In the first set of simulations, ellipsoidal particles are initially distributed with a uniform concentration between 1 and 30 wall units and particle trajectories are evaluated for a duration of 100 wall units of time. The streamwise direction is along the x-coordinate and $y^+ = \pm 125$ are the locations of the side walls. For $u^* = 0.3$ m/s, $S = 1000, \beta = 5$ in a horizontal duct, sample variations of the number of deposited particles versus time for different minimum diameters are shown in Fig. 3. It is observed that the number of deposited particles increases with particle

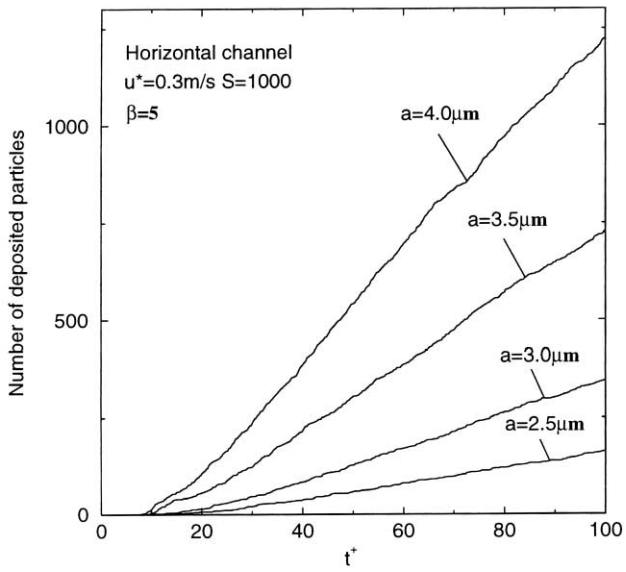

Fig. 3. Variations of the number of deposited ellipsoidal particles versus time.

diameter in the size range shown in this figure. Also the rate of particle deposition reaches its equilibrium limit after about 30 wall units of time.

7.1. Concentration profiles

The variation of particle concentration in turbulent dilute channel flows is also studied. Ensembles of 15,000 ellipsoidal particles are initially uniformly distributed across the entire channel with random orientations. For a fixed equivalent particle relaxation time of $\tau_{eq}^{+} = 2.26$ and different aspect ratios, β, the time evolution of concentration is studied. The trajectories of particles were computed in a time period of 0–300 wall units. The concentration $C(y)$ is evaluated by $C(y) = N_y/N$, where N_y is the number of particles in the region $[y, y + \Delta y]$ and N is the total number of particles. In these calculations, a bin size of $\Delta y = 0.25$ wall units is considered and the concentrations at different times ($t^{+} = 0, 100, 200$ and 300) are plotted in Figs. 4(a)–(c). The results for spherical particles with $d = 10$ μm ($d^{+} = 0.2, \tau^{+} = 2.26$), and ellipsoidal particles with $\beta = 5$ ($a = 3.33$ μm, $a^{+} = 0.067$) and $\beta = 10$($a = 2.95$ μm, $a^{+} = 0.059$) are shown in these figures. Here a particle-to-fluid density ratio of $S = 1000$ and a shear velocity of $u^{*} = 0.3$ m/s are assumed.

Fig. 4 shows that both spherical and ellipsoidal particles tend to drift toward the wall and to accumulate in the viscous sublayer. This is because particles are thrown into the viscous sublayer by the down sweep motion of near wall turbulent eddies, and since the intensity of velocity fluctuations normal to the wall is very small in the viscous sublayer, particles have large residence times in this region. Earlier Squires and Eaton (1991b) reported that the spherical particles collect preferentially in regions of low vorticity and high strain rate. McLaughlin (1989), Li and Ahmadi (1993) and Fan and Ahmadi (2000) observed a similar accumulation of spherical particles in the

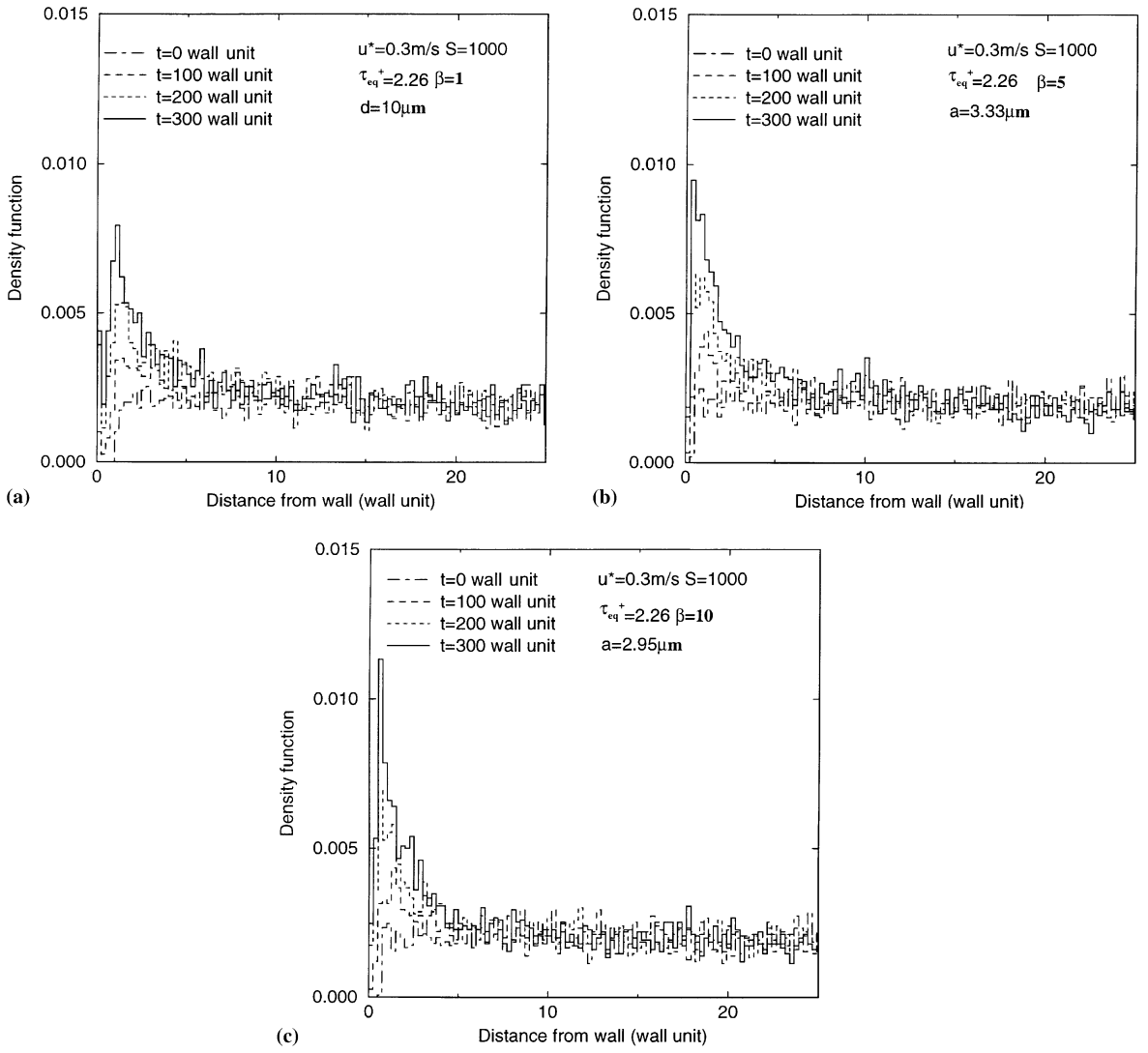

Fig. 4. Variations of the particle concentration near the lower wall at different times: (a) spherical particles; (b) ellipsoidal particles with $\beta = 5$; (c) ellipsoidal particles with $\beta = 10$.

viscous sublayer. In particular McLaughlin showed that a particle spends about 300 wall units of time in the viscous sublayer and this behavior is typical of particles in this region. Figs. 4(a)–(c) also show that the rate of accumulation in the sublayer increases with particle aspect ratio. That is, particles with large aspect ratio are more easily caught by the turbulence near wall eddies.

7.2. Initial location of deposited particles

The well-known streaky structures of turbulent near wall flows were summarized by Hinze (1975) and Smith and Schwartz (1983). In the earlier works of Ounis et al. (1993) and Soltani

and Ahmadi (1995), it was shown that the turbulence near wall coherent eddies play a dominant role in particle deposition and resuspension processes. To study the effect of coherent eddy structures on elongated particle deposition, a simulation is performed with particle initial positions being uniformly distributed in a region with a width of 12 wall units from the wall, which covers the peak fluctuation energy production region. Here, the effect of gravity is neglected and $S = 1000, u^* = 0.3$ m/s are assumed in the simulations. Figs. 5(a), (b) and (c), respectively, show the initial locations of the deposited 15 μm ($d^+ = 0.3$) spherical particles and

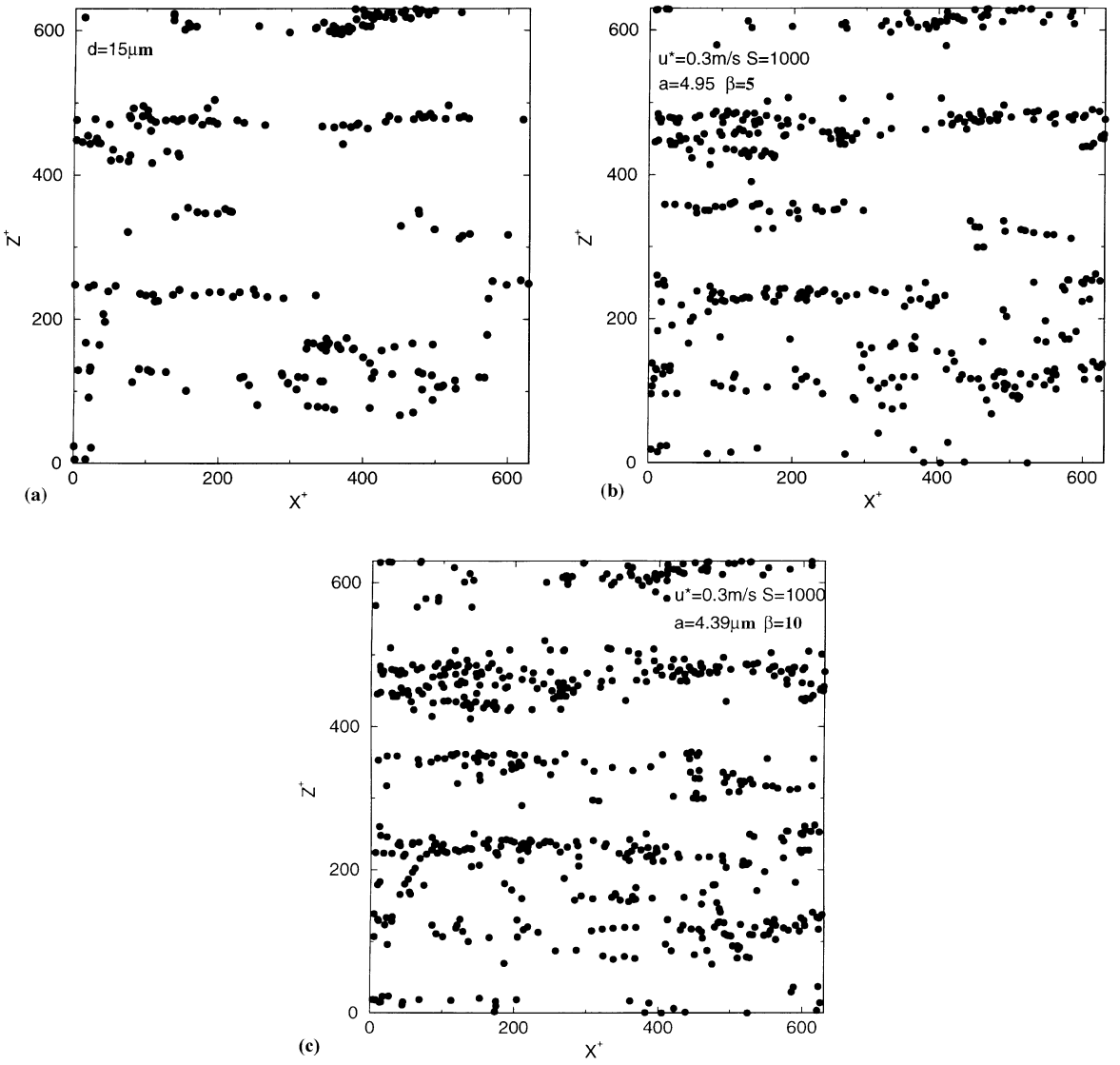

Fig. 5. Distribution of the initial locations of deposited particles in the x–z plane: (a) spherical particles; (b) ellipsoidal particles with $\beta = 5$; (c) ellipsoidal particles with $\beta = 10$.

ellipsoidal particles with $a = 4.95$ μm $(a^+ = 0.099), \beta = 5$ and $a = 4.39$ μm $(a^+ = 0.088), \beta = 10$, in a time duration of 0–100 wall units. Note that these different groups of particles have a relaxation time of $\tau_{eq}^+ = 5.0$. Fig. 5 shows that the initial locations of deposited spherical and ellipsoidal particles in the x–z plane are concentrated on certain bands which are about 100 wall units apart. This shows that the near wall streamwise eddies play an important role for deposition of both spherical and ellipsoidal particles. This figure also shows that the number of the deposited particles increases with the aspect ratio for a fixed equivalent relaxation time. Furthermore, the band widths in Figs. 5(b) and (c) are larger than those in Fig. 5(a). That is, more of the ellipsoidal particles are entrained into the near wall eddies when compared with spherical particles. Thus, the bands of the initial locations of deposited particles are more cluttered for elongated particles.

To provide information on the effect of aspect ratio on particle transport and deposition near the wall, sample particle trajectories are studied. Figs. 6(a) and (b), show the sample trajectories of spherical and ellipsoidal particles with the same initial locations. Here, the same simulation condition is used and the initial location is selected from Fig. 5. It is observed that spherical and ellipsoidal particles follow almost the same path at first up to y^+ of about 7 and then they diverge. The ellipsoidal particles deposit on the wall, while the spherical particle moves away. This figure shows that the particle aspect ratio plays a major role in the transport and deposition of ellipsoids in turbulent flows.

To shed light on the preferential concentration of ellipsoidal particles in the viscous sublayer, a set of simulations is performed. Particles are initially uniformly distributed in the region with 30 wall units from the lower wall. The effect of gravity is neglected, $S = 1000$, $u^* = 0.3$ m/s are assumed, and an ensemble of 8192 ellipsoidal particles with $a =$ 4.95 μm $(a^+ = 0.099), \beta = 5$ is used. Figs. 7(a)–(c) show the instantaneous locations of ellipsoidal particles in the y–z plane at different times. These figures show that particle concentration in the y–z plane is nonuniform and that the ellipsoids tend to accumulate in certain regions near the wall due to the turbulence coherent eddy structures. High concentration regions form near the wall, and particles seem to concentrate in bands at z^+ of about 100, 200–220, 300, 410 and 550. The distances between the consecutive high density bands are about 100–130. While the particle distribution structure smears out in time due to the movements of the coherent eddies, similar patterns are still noticeable at $t^+ = 200$ in Fig. 7(c) in the viscous sublayer region.

The corresponding instantaneous particle locations in the x–z plane at different times are shown in Fig. 8. At $t^+ = 50$, Fig. 8(a) shows that for $x^+ < 800$, there are bands of high concentration regions along the x-axis whose locations are comparable to those of Fig. 7. For $x^+ > 800$, particles disperse and the structure in the density distribution tends to smear out. Similar structures are also seen in Fig. 8(b) for $t^+ = 100$ wall units. The observations of these nonuniform elongated particle distributions are consistent with the earlier studies for spheres. Squires and Eaton (1991b) found that the spherical particles collect preferentially in regions of low vorticity and high strain rate. The periodic streaky concentration with a spacing of about 100–150 wall units in the viscous sublayer was also reported by Soltani and Ahmadi (1995). Figs. 7 and 8 indicate that the near wall eddy structure plays an important role in the ellipsoidal particle transport and the ellipsoidal particles tend to accumulate in certain bands due to the turbulent near wall eddy structures with a spacing of about 100–150 wall units.

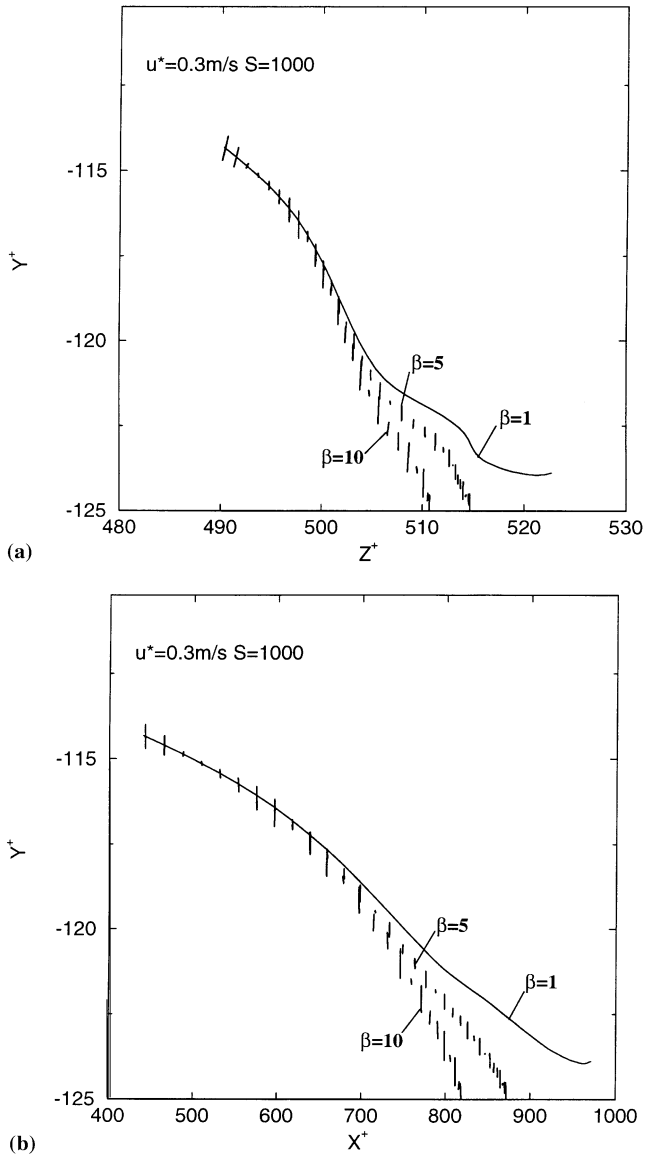

Fig. 6. Samples of trajectories for spherical and ellipsoidal particles: (a) y–z plane; (b) x–y plane.

7.3. Point and plane source

For $\tau_{eq}^{+} = 5.0$, the trajectory statistics for spherical particles ($d = 15$ μm, $d^{+} = 0.3$) and ellipsoidal particles ($\beta = 5, a = 4.95$ μm, $a^{+} = 0.099$, and $\beta = 10, a = 4.39$ μm, $a^{+} = 0.088$) released from a point source at a distance of five wall units from the lower wall at $x^{+} = 304.95, z^{+} = 237.25$ are shown in Fig. 9. The point source is selected in the region that the near wall eddies form a jet flow toward the wall. Here, $S = 1000$, $u^{*} = 0.3$ m/s, $g^{+} = 0$ and 8192 samples are used. The

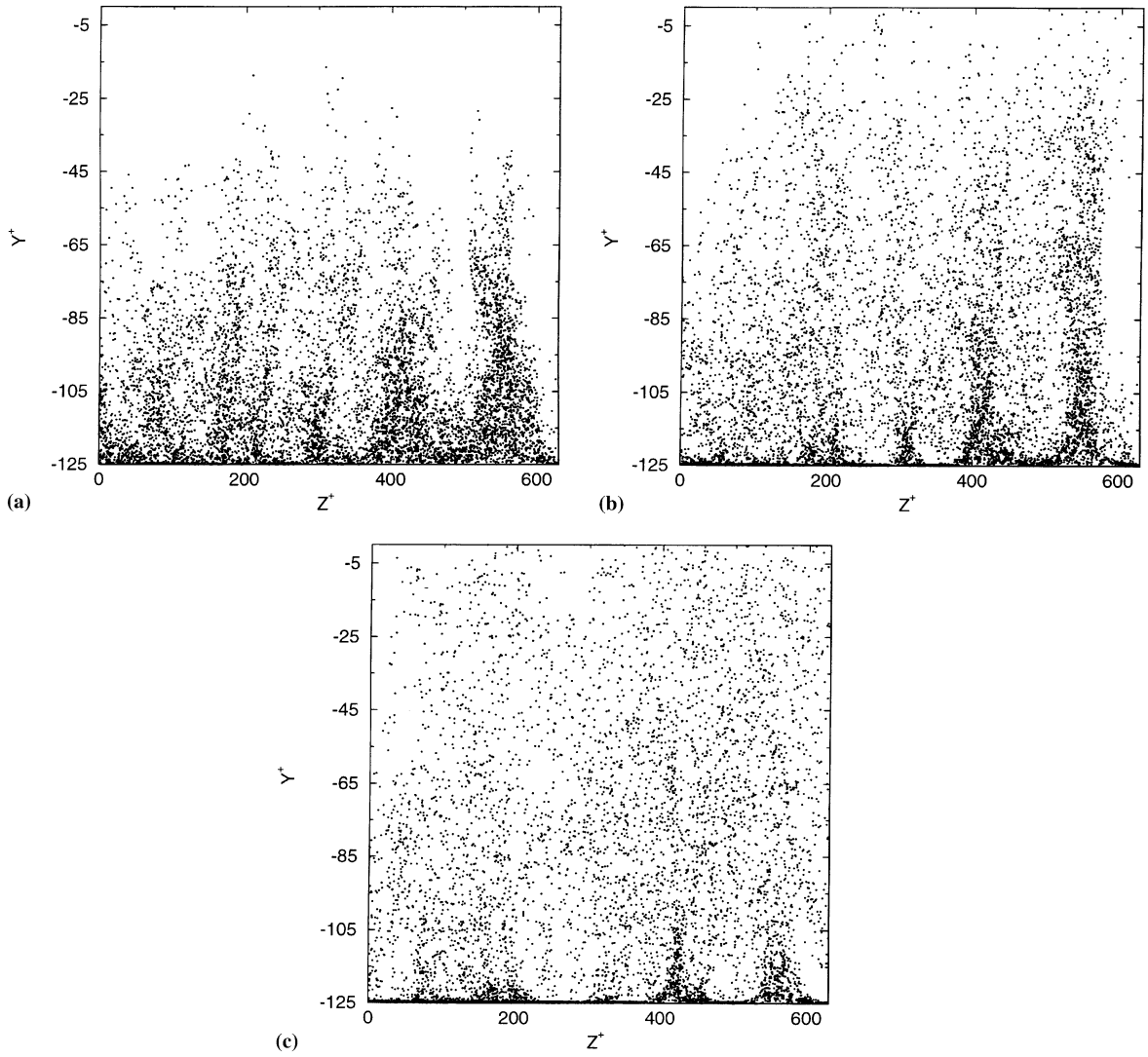

Fig. 7. Distribution of ellipsoidal particles: (a) y–z plane at $t^+ = 50$; (b) y–z plane at $t^+ = 100$; (c) y–z plane at $t^+ = 200$.

initial orientations of ellipsoids are picked randomly from a uniform distribution. Fig. 9 shows that the ellipsoidal particles disperse due to their random initial orientations. For these large particles, the Brownian dispersion is negligible and the spherical particles almost follow the same path. Fig. 9(a) indicates that after about 30 wall units of times all spherical particles deposit. While ellipsoidal particles exhibit significant dispersion, their mean path is quite similar to that of spherical particles for $t^+ < 20$. Figs. 9(b) and (c) show that ellipsoidal particles with $\beta = 5$, and $\beta = 10$ begin to deposit at about 20 and 15 wall units of time, respectively. Comparing Figs. 9(b) and (c) shows that the dispersion rate of ellipsoidal particles increases as the aspect ratio increases.

Sample trajectories statistics for three ellipsoidal particles with $\beta = 5$, $a = 4.95$ μm ($a^+ = 0.099$) emitted from the point source with different orientations are shown in Fig. 10. It is

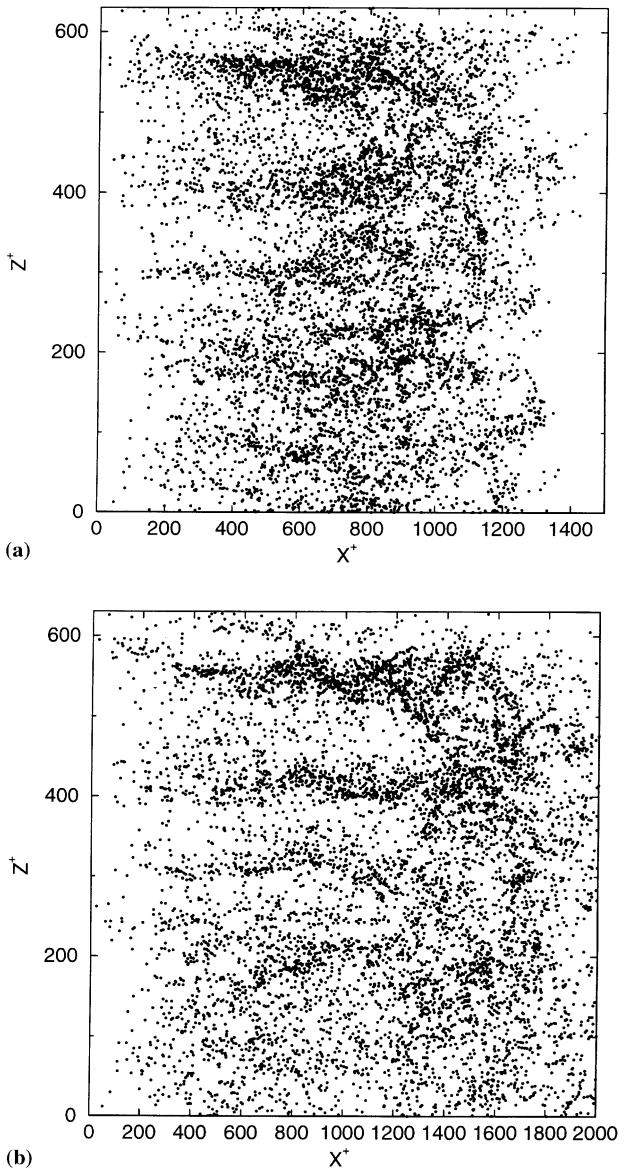

Fig. 8. Distribution of ellipsoidal particles: (a) x–z plane at $t^+ = 50$; (b) x–z plane at $t^+ = 100$.

observed that the particles initially follow roughly the same path, then disperse due to the different orientations and finally deposit on the lower wall.

In the next set of simulation, dispersion and deposition of spherical and ellipsoidal particles that are initially released from a plane source at a distance of 5 wall units from the lower wall with randomly distributed orientations in the absence of gravity are studied. An ensemble of 8192 particles with $\tau_{eq}^+ = 5.0$, $S = 1000, u^* = 0.3$ m/s and different aspect ratios is used in these simulations. Fig. 11 shows that spherical and ellipsoidal particles with the same relaxation time and

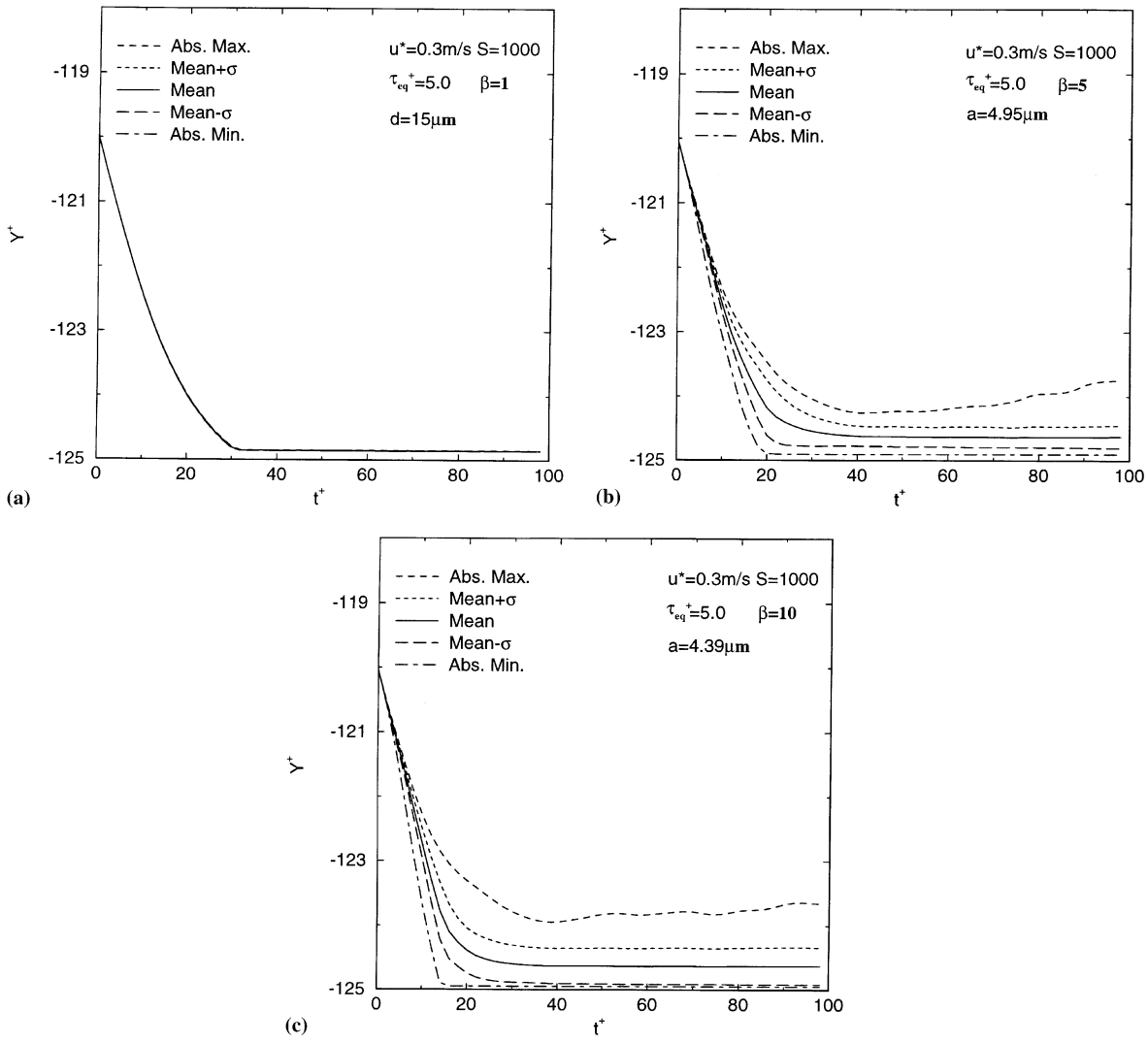

Fig. 9. Trajectory statistics for particles released from a point source: (a) spherical particles; (b) ellipsoidal particles with $\beta = 5$; (c) ellipsoidal particles with $\beta = 10$.

different aspect ratios have similar dispersion statistics. That is, the transport of particles with relatively large relaxation times is almost entirely governed by the turbulent flows, and the particle aspect ratio contributes only slightly to their dispersion process.

7.4. Deposition velocity

In this section a series of simulations for ellipsoidal particle deposition in vertical and horizontal ducts are performed. The effect of aspect ratio and gravity on the elongated particle deposition rate is studied. Three cases of absence of gravity, a vertical duct with gravity in the flow

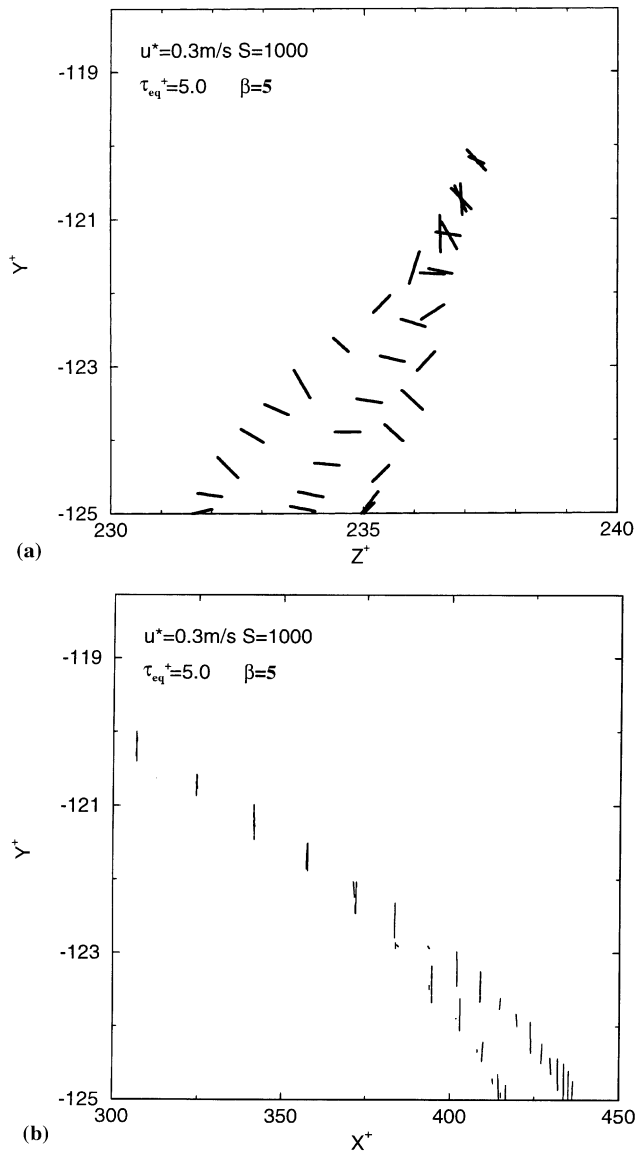

Fig. 10. Samples of trajectories for ellipsoidal particles emitted from a point source: (a) y–z plane; (b) x–y plane.

direction, and a horizontal channel with gravity toward the lower wall are studied. The resulting deposition velocities for different particle sizes, aspect ratios and flow shear velocities are tabulated in Tables 1–3. In this section, the results are compared with the experimental data for spherical particles and elongated fibers.

Fig. 12(a) shows the variation of deposition velocity of ellipsoidal particles versus equivalent relaxation times. A value of $u^* = 0.3$ m/s, $S = 1000$ and the equivalent relaxation time as given by Eq. (48) is used. The experimental data collected by Papavergos and Hedley (1984) for deposition rate of spherical particles in vertical ducts are shown by small dots in this figure. The sublayer

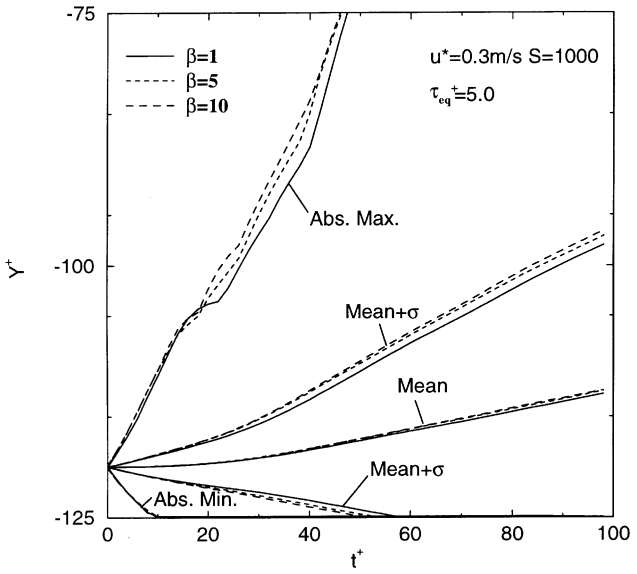

Fig. 11. Fiber trajectory statistics for particles released from a plane source.

model predictions of Fan and Ahmadi (1995c), the DNS results for deposition velocity of spherical particles as reported by Zhang and Ahmadi (2000) and the empirical equation predictions given by Eq. (53) are also reproduced in Fig. 12(a) for comparison. It is observed that the DNS results are in close agreement with the sublayer model and the empirical equation. In the absence of gravity, Fig. 12(a) clearly shows that as the particle aspect ratio increases, the deposition velocity for $0.5 < \tau_{eq}^{+} < 10$ increases significantly. This is because deposition by the interception mechanism becomes very efficient for elongated particles. As expected, Fig. 12(a) also shows that the deposition velocity for ellipsoidal particles with $\beta = 5$ in the vertical channel with downward flow is somewhat larger than that in the absence of gravity. In this case, the gravity tends to increase the velocity of particles in the streamwise direction and thus increases the lift force toward the wall (Fan and Ahmadi, 1993). For the floor deposition in a horizontal channel, Fig. 12(a) shows that the gravity significantly enhances ellipsoidal particle deposition rate.

Fig. 12(b) shows the computer simulation results for variations of deposition velocity with equivalent relaxation time for ellipsoids with different aspect ratios and $S = 1000$ in flows with $u^* = 0.1$ m/s. The cases where gravity is absent and when it is in the flow direction or perpendicular to the lower wall are studied. The earlier DNS results of Zhang and Ahmadi (2000) and the predictions of Eq. (53) are also shown in this figure for comparison. It is observed that the empirical model is in good agreement with the DNS results. Similar to Fig. 12(a), the increase of particle aspect ratio leads to an increase in the deposition velocity, and gravity enhances the deposition rate. Comparing Figs. 12(a) and (b) shows that the effect of particle aspect ratio is more pronounced at low shear velocities. That is, the deposition velocity difference for $\beta = 2$ and $\beta = 5$ for flows with $u^* = 0.1$ m/s is much larger than that for $u^* = 0.3$ m/s. The effect of gravity is also more significant at lower shear velocities for both vertical and horizontal channels. In particular, gravity significantly increases the deposition velocity in the horizontal channel. It should be

Table 1
Deposition velocity[a]

a (μm)	$\beta = 1$ $g = 0$	$\beta = 1$ Vertical duct	$\beta = 1$ Horizontal duct	$\beta = 2$ $g = 0$	$\beta = 5$ $g = 0$	$\beta = 5$ Vertical duct	$\beta = 5$ Horizontal duct
2.5	–	–	3.36e−3	–	–	–	9.15e−3
2.8	–	–	–	–	–	2.92e−3	1.75e−2
3.0	–	–	–	–	–	–	2.23e−2
3.2	–	–	–	–	2.56e−3	5.12e−3	3.00e−2
3.5	–	–	8.21e−3	–	4.11e−3	1.17e−2	3.80e−2
3.7	–	–	–	–	–	–	4.57e−2
4.0	–	–	–	3.71e−4	1.10e−2	2.92e−2	6.07e−2
4.5	–	–	–	8.60e−4	2.45e−2	4.83e−2	–
5.0	4.84e−4	4.84e−4	1.36e−2	3.66e−3	4.22e−2	6.95e−2	–
5.5	1.47e−3	1.60e−3	1.81e−2	7.32e−3	–	–	–
6.0	3.91e−3	4.08e−3	2.26e−2	1.47e−2	–	–	–
6.25	–	9.16e−3	–	–	–	–	–
6.5	1.44e−2	–	3.09e−2	–	–	–	–
7.0	2.04e−2	2.22e−2	3.09e−2	3.29e−2	–	–	–
7.25	–	3.14e−2					
7.5	6.56e−2	–	0.140	–	–	–	–
8.0	0.109	–	0.229	–	–	–	–
25.0	0.128	0.134	0.266	–	–	–	–

[a] (u_d^+) $u^* = 0.3$ m/s, $S = 1000$.

emphasized here that the nondimensional acceleration of gravity given by Eq. (44) is inversely proportional to the cubic power of shear velocities. Thus, the effect of gravity increases markedly as the shear velocity decreases. This observation is consistent with the results of Zhang and Ahmadi (2000) for spherical particles.

Figs. 12(a) and (b) show that for the nearly spherical particles, the simulation results for $u^* = 0.3$ m/s are in better agreement with the collection of experimental data of Papavergos and Hedley (1984) when compared with those for $u^* = 0.1$ m/s. This is because, these data which are mainly for spherical particles in vertical ducts are conducted at air velocities more than 4 or 5 m/s. Therefore, u^* is about 0.3 larger for most of the experimental data reported in these figures.

Available experimental data for deposition rates of fibers in turbulent flows are rather limited. Only Shapiro and Goldenberg (1993) reported their data for the deposition velocity of glass fibers with $\rho^p = 2230$ kg m^{-3}, averaged diameters of 1.86 μm and various lengths ranging from 2 to 50 μm in a horizontal duct. They used three flow Reynolds numbers: $Re = 3.0 \times 10^4, 5.4 \times 10^4$, and 8.7×10^4 (corresponding to $u^* \approx 0.6$, 1.0 and 1.6 ms^{-1}, respectively). Kvasnak and Ahmadi (1995) measured the floor deposition rates for glass fibers in a horizontal channel with a rectangular cross-section area of 15.25×2.54 cm^2. The flow Reynolds number based on the hydraulic diameter of the channel was 1.7×10^4 which corresponded to a friction velocity of 0.27 ms^{-1}. The diameter of the glass fibers in these experiments was 5 μm ($d^+ = 0.09$) and the fiber lengths varied from 20 to 100 μm. A series of computer simulations with conditions identical to those of the experiments are performed and the results are compared with the experimental data for ellipsoidal particle deposition velocity in Fig. 13.

Table 2
Deposition velocity[a]

a (μm)	$\beta = 1$ $g = 0$	$\beta = 1$ Vertical duct	$\beta = 1$ Horizontal duct	$\beta = 2$ $g = 0$	$\beta = 5$ $g = 0$	$\beta = 5$ Vertical duct	$\beta = 5$ Horizontal duct
2.1	–	–	–	–	–	–	2.42e−2
2.5	–	–	3.93e−3	–	–	–	2.87e−2
3.0	–	–	8.12e−3	–	–	–	3.96e−2
4.0	–	–	1.21e−2	–	–	–	6.59e−2
5.0	–	–	2.03e−2	–	–	–	9.74e−2
6.0	–	–	–	–	–	8.79e−3	1.13e−1
7.0	–	–	–	–	–	1.17e−2	–
7.5	–	1.76e−3	4.42e−2	–	–	–	–
8.0	–	–	–	–	–	2.12e−2	–
9.0	–	–	–	–	1.47e−3	3.74e−2	–
9.5	–	–	–	–	4.39e−3	–	–
10.0	–	3.84e−3	7.40e−2	–	7.32e−3	5.05e−2	–
11.0	–	–	–	–	1.47e−2	7.98e−2	–
12.0	–	–	–	–	2.86e−2	–	–
12.5	–	–	1.04e−1	–	–	–	–
13.0	–	8.56e−3	–	3.29e−3	–	–	–
13.5	–	–	–	5.13e−3	3.37e−2	–	–
14.0	–	9.16e−3	–	–	–	–	–
14.5	–	–	–	1.10e−2	–	–	–
15.0	–	1.49e−2	1.29e−1	–	6.08e−2	–	–
16.0	9.92e−4	–	–	1.50e−2	–	–	–
17.0	–	–	–	2.05e−2	–	–	–
17.5	2.74e−3	3.81e−2	1.43e−1				
19.0	–	–	–	3.41e−2	–	–	–
20.0	1.01e−2	5.13e−2	1.50e−1				
22.0	–	–	–	6.30e−2	–	–	–
25.0	3.55e−2	1.03e−1	1.56e−1	–	–	–	–
30.0	8.62e−2	–	–	–	–	–	–
32.0	–	–	–	–	–	–	–
35.0	1.11e−1	–	–	–	–	–	–
40.0	1.41e−1	–	–	–	–	–	–

[a] (u_d^+) $u^* = 0.1$ m/s, $S = 1000$.

For a particle-to-fluid density ratio of $S = 1820$ and a semi-minor axis of 0.93 μm and different major axis lengths, the direct numerical simulation (DNS) results for nondimensional deposition velocities on the duct side wall and the floor are shown in Fig. 13 and the results are compared with the experimental data of Shapiro and Goldenberg. A comparison of the computer simulation results with the floor deposition data of Kvasnak and Ahmadi (1995) is also shown in this figure. Here, $S = 1820$, $u^* = 0.27$ m/s, and $a = 2.5$ μm are used in the simulation. It is observed that the simulation results are in good agreement with the experimental data. The sublayer model predictions of Fan and Ahmadi (1995a) are also reproduced in this figure which shows a general agreement with the simulation results and the experimental data.

Fig. 13 also shows that the floor deposition velocity is a strong function of shear velocity. Some of the experimental data of Shapiro and Goldenberg (1993) and Kvasnak and Ahmadi (1995) are

Table 3
Deposition velocity[a]

β	$u^* = 0.27$ m/s, $a = 2.5$ μm Horizontal duct	$u^* = 0.6$ m/s, $u^* = 1.0$ m/s, $a = 0.93$ μm $g = 0$	$u^* = 1.0$ m/s, $a = 0.93$ μm Horizontal duct	$u^* = 1.6$ m/s, $a = 0.93$ μm Horizontal duct
2.15	–	–	–	4.83e−2
3.23	–	–	–	8.13e−2
3.76	–	–	–	0.11
4.0	2.38e−2	–	–	–
4.3	–	–	2.05e−2	–
5.37	–	–	–	0.14
8.0	3.30e−2	–	–	–
8.6	–	–	3.96e−2	–
10.8	–	–	–	0.18
16.0	4.21e−2	–	–	–
17.2	–	7.47e−4	5.32e−2	–
21.5	–	1.87e−3	–	–
24.0	5.12e−2	–	–	–
30.0	–	3.82e−3	7.17e−2	–
32.0	6.59e−2	–	–	–
40.0	7.32e−2	–	–	–
60.0	–	1.13e−2	–	–
100.0	–	2.82e−2	–	–

[a] $(u_d^+)S = 1820$.

in the same range of τ_{eq}^+. However, the floor deposition velocities reported by Kvasnak and Ahmadi (1995) are much higher than those of Shapiro and Goldenberg (1993) even though the interception effect in the former experiment is expected to be less significant than the later one. This is because the nondimensional acceleration of gravity, $\mathbf{g}^+$, as given by Eq. (44), is proportional to u^{*-3}. Therefore, the gravitational enhancement of deposition rate at low shear velocities is much larger than that for flows with high shear velocities. This trend of variations for spherical particle was reported earlier by Zhang and Ahmadi (2000).

Variations of the deposition velocity as predicted by the empirical equation given by Eq. (53) are also shown in Fig. 13. It is observed that the empirical equation predicts the trend of variations of the experimental data. The model predictions however, deviate from the experimental data for horizontal channels for certain ranges, and overestimates the side deposition.

7.5. Motion statistics

In this section several simulations are performed and the orientation and the angular velocity distribution of ellipsoidal particles in turbulent channel flows are studied. An ensemble of 8192 particles with $\tau_{eq}^+ = 5.0$, $S = 1000$, and different shear velocities, aspect ratios, and gravity directions are used in these simulations. Specifically, $a = 4.95$ μm $(a^+ = 0.099)$, $\beta = 5$ for ellipsoidal particles and $d = 15$ μm $(d^+ = 0.3)$ for spherical particles for flows with $u^* = 0.3$ m/s, and $a = 14.8$ μm $(a^+ = 0.099)$, $\beta = 5$ for ellipsoidal particles and $d = 45$ μm $(d^+ = 0.3)$ for spherical particles for $u^* = 0.1$ m/s are used. For all these cases, the nondimensional particle relaxation time is $\tau_p^+ = 5$. Particles are initially uniformly distributed with random orientations in the region

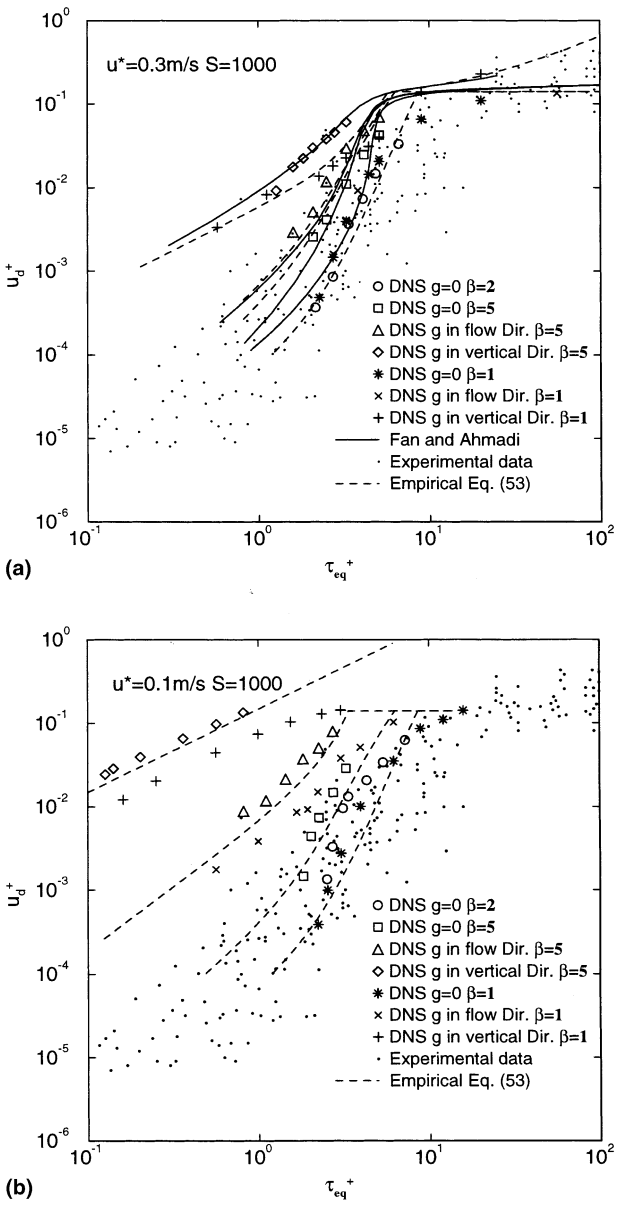

Fig. 12. Variations of deposition velocity with particle relaxation time and aspect ratios for different shear velocities: (a) $u^* = 0.3$ m/s; (b) $u^* = 0.1$ m/s.

within 30 wall units from the lower wall. All statistical values are evaluated using the ensemble of particles that are moving in the viscous sublayer and part of buffer layer (within 12 wall units from the lower wall) in a time duration of 100 wall units.

Figs. 14(a) and (b), respectively, show variations of orientation density functions for ellipsoidal particle with $\beta = 5$ moving in the region within 12 wall units from the lower wall for u^* of 0.3 and 0.1 m/s. The cases that the gravity is absent or present are analyzed. The density function is

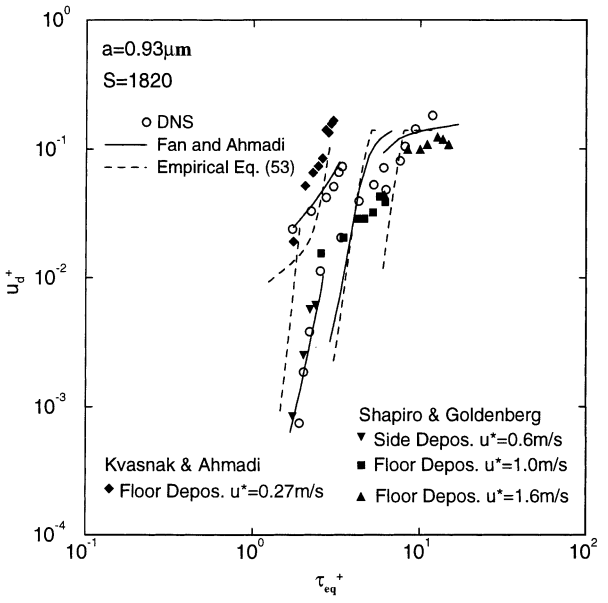

Fig. 13. Comparisons of the simulation results with the experimental data, sublayer model predictions and empirical model.

computed by $f(\xi) = N_\xi/N$, where $\xi = |\cos(\theta)|$, and θ being the angle between the axis of the ellipsoidal particle ($\hat{z}$-axis in the particle coordinate) and coordinate axis x, y, and z. Here, N_ξ is the number of particles with ξ in the region $[\xi, \quad \xi + \Delta\xi]$, $\Delta\xi = 0.005$ and N is the total sample number used. Note that the density function satisfies the normalization condition, $\sum_{i=1}^{200} f(\xi_i) = 1$. It is observed that $|\cos(\theta_x)|$ has a roughly uniform distribution between 0 and 0.8 and has a high peak near 1.0, which indicates that the ellipsoids tend to align themselves with the direction of motion (x-axis). The distributions of $|\cos(\theta_y)|$ and $|\cos(\theta_z)|$ have their main peaks at 0 and their secondary peaks at 1.0 with a gradual variation in between. Fig. 14(a) also shows that the effect of gravity on the motion of ellipsoids at shear velocity of $u^* = 0.3$ m/s is negligible. Fig. 14(b) shows the orientation distribution results for $u^* = 0.1$ m/s. It is observed that the trends of orientation distributions are very similar to that for $u^* = 0.3$ m/s, and elongated particles tend to orient themselves along the flow direction. The presence of gravity in the flow direction at low shear velocity of $u^* = 0.1$ m/s, however, affects the lateral orientation distributions, but does not alter the statistics of $|\cos(\theta_x)|$.

Variations of mean and RMS values of orientation statistics in the wall region with distance from the wall are shown in Fig. 15. For $u^* = 0.3$ m/s, Fig. 15(a) shows that the mean value of $|\cos(\theta_x)|$ remains roughly constant across the sublayer, while $\overline{|\cos(\theta_y)|}$ decreases and $\overline{|\cos(\theta_z)|}$ increases with distance from the lower wall in the viscous sublayer. Mean orientations tend to remain almost constant after 10 wall units from the wall. It is also observed in Fig. 15(a) that the mean value of $|\cos(\theta_x)|$ is about twice as those of $|\cos(\theta_y)|$ and $|\cos(\theta_z)|$, which indicates that the ellipsoids tend to have their major axis parallel to the x-direction. The effect of gravity in this figure is negligible. Fig. 15(b) shows variations of average orientations for $u^* = 0.1$ m/s. The

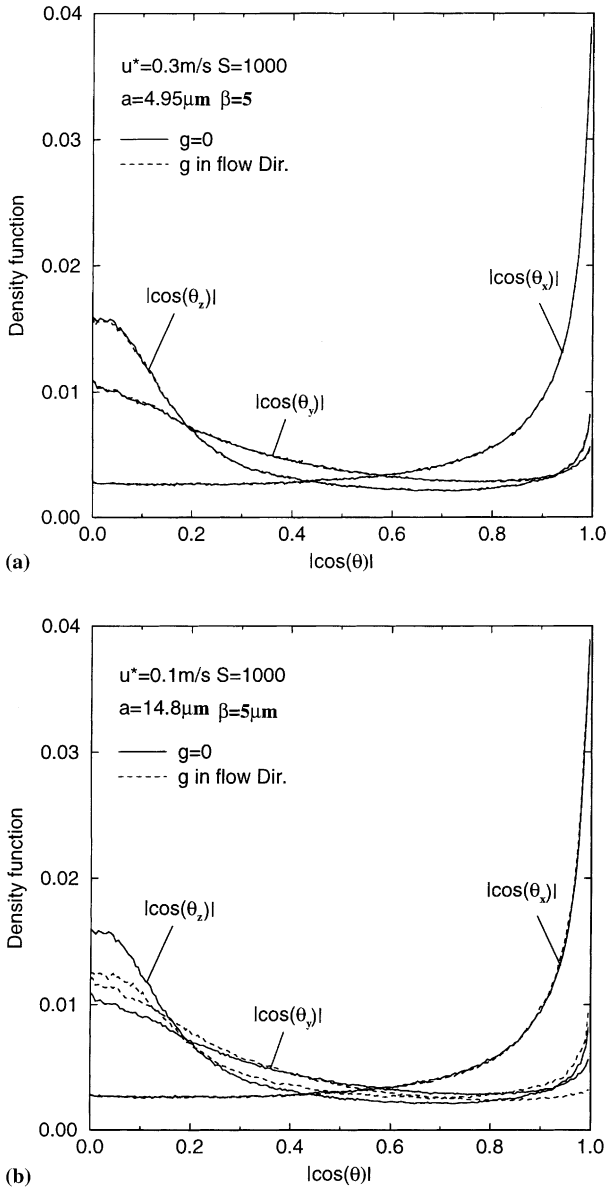

Fig. 14. Variations of orientation density functions for ellipsoidal particles with $\beta = 5$: (a) $u^* = 0.3$ m/s; (b) $u^* = 0.1$ m/s.

results are similar to those in Fig. 15(a), except that the lateral orientation distributions of ellipsoids become more similar when gravity is in the flow direction.

Figs. 15(c) and (d), respectively, show the RMS orientation statistics in the wall region. It is observed that the distributions of RMS of $|\cos(\theta_x)|$ and $|\cos(\theta_z)|$ are about 0.3 and remain constant near the wall. The RMS of $|\cos(\theta_y)|$ is somewhat smaller and has a decreasing trend up to about 10 wall units from the wall and remains roughly constant or increases slightly afterward. It is also observed that the effect of gravity on RMS orientation is negligible.

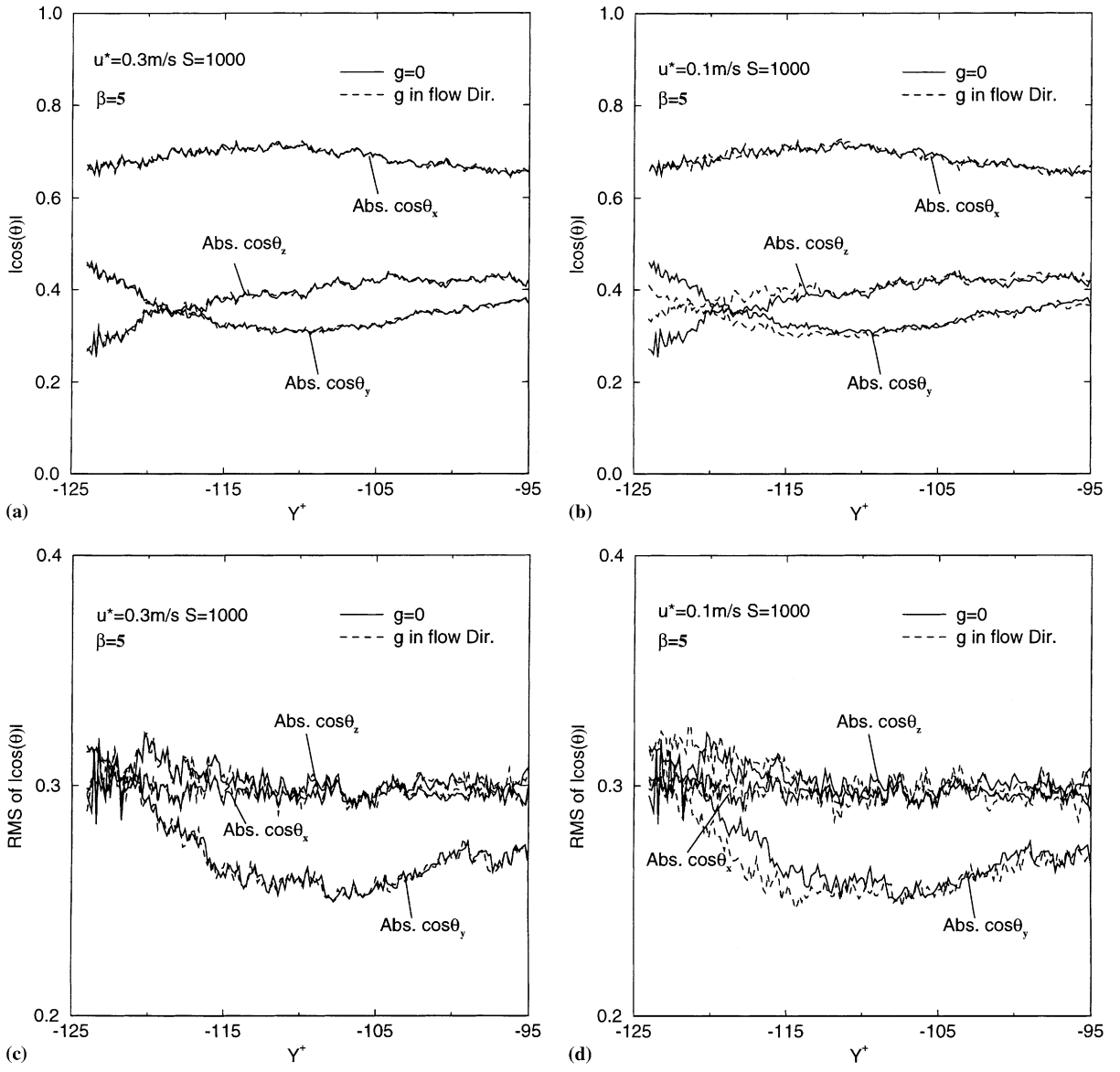

Fig. 15. Variations of mean and RMS orientations near wall for ellipsoidal particles with $\beta = 5$: (a) mean orientations for $u^* = 0.3$ m/s; (b) mean orientations for $u^* = 0.1$ m/s; (c) RMS orientations for $u^* = 0.3$ m/s; (d) RMS orientations for $u^* = 0.1$ m/s.

The distribution functions of the absolute value of angular velocities of ellipsoidal particles with $\beta = 5$ in the wall region are shown in Fig. 16. The method used for evaluating the density function is the same as that used for the orientation distribution. (Here, a value of $\Delta\omega = 0.005$ is used.) It is observed that the angular velocity about the z-axis is comparatively larger than those about the other axes. The angular velocity about the y-axis is the smallest. That is, ellipsoidal particles

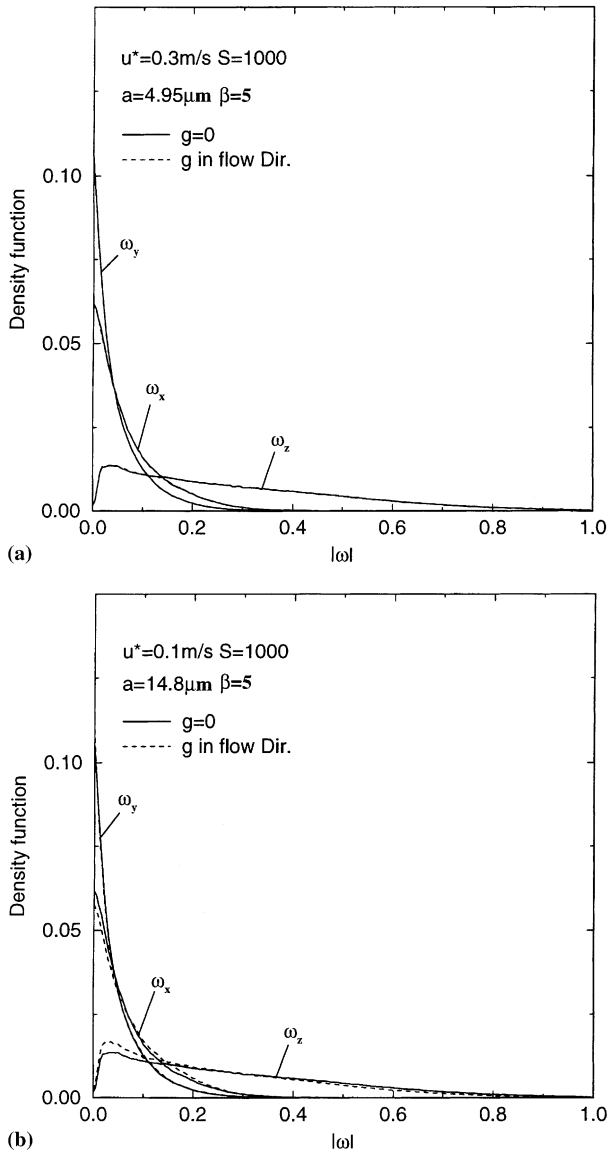

Fig. 16. Variations of angular velocity density function for ellipsoidal particles with $\beta = 5$: (a) $u^* = 0.3$ m/s; (b) $u^* = 0.1$ m/s.

generally rotate about the z-axis due to the streamwise mean shear field with little rotation about the y-axis perpendicular to the shear field. Fig. 16(b) shows the similar trend of distribution of angular velocity for $u^* = 0.1$ m/s. The presence of gravity, however, slightly affects the angular velocity distributions, while it has no effect at high shear velocities.

Variations of mean streamwise velocities and the fluctuation velocities of spherical and ellipsoidal particles in the wall region are shown in Fig. 17. Fig. 17(a) shows that the mean velocity of

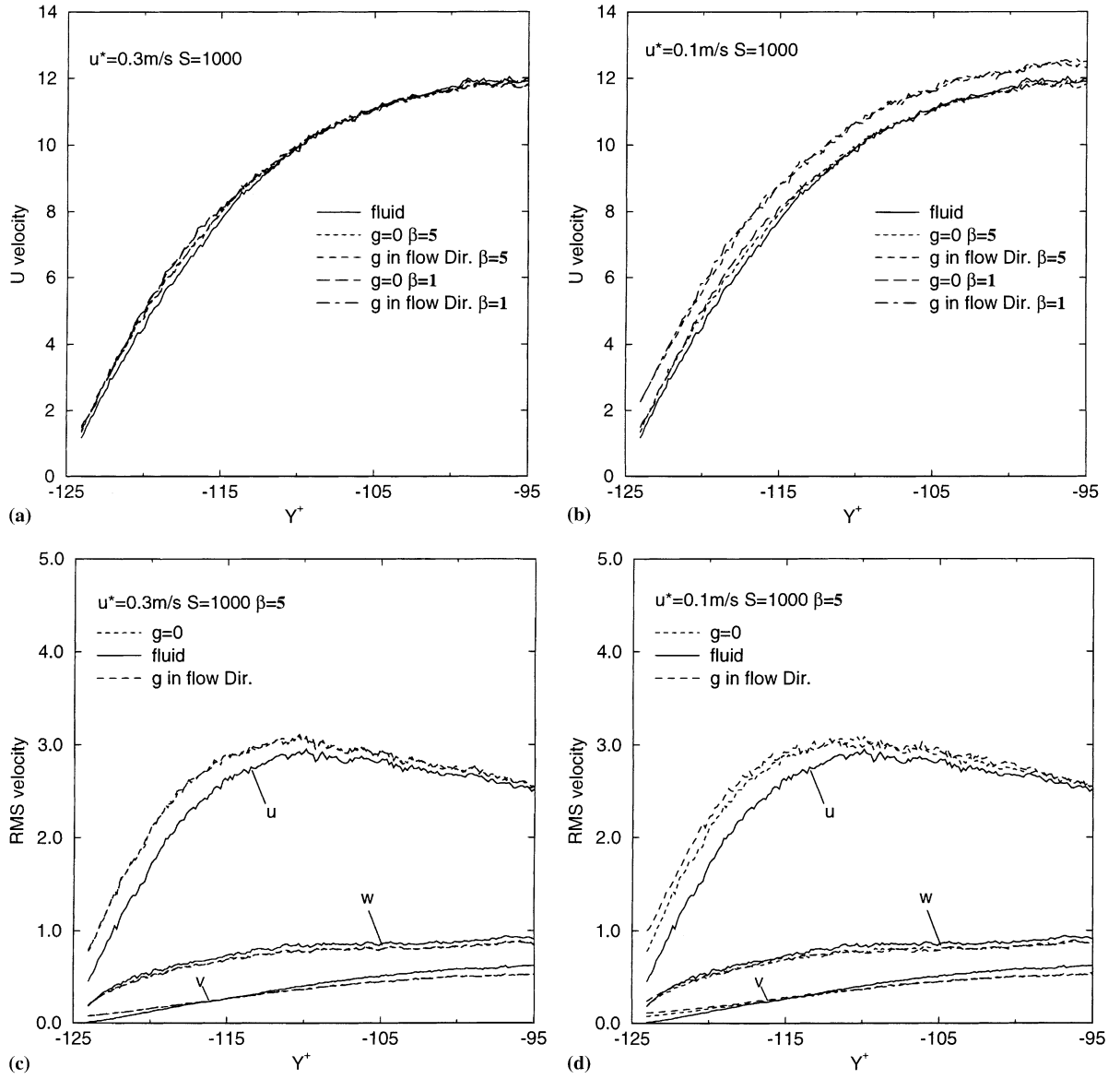

Fig. 17. Variations of mean and RMS velocities of fluid and particles near the wall for different shear velocities: (a) mean velocities for $u^* = 0.3$ m/s; (b) mean velocities for $u^* = 0.1$ m/s; (c) RMS velocities for $u^* = 0.3$ m/s; (d) RMS velocities for $u^* = 0.1$ m/s.

spherical and ellipsoidal particles in the streamwise direction is larger than that of the fluid even in the absence of gravity. A similar behavior for spherical particles was reported in the earlier work of Zhang and Ahmadi (2000). The reason is that the particles are drifting toward the wall (perhaps by the down sweep motion of the coherent eddies), and they carry their larger streamwise velocities compared to that of the surrounding fluid. Fig. 17(a) also shows when gravity is in the flow

direction, the mean velocity of particles in the streamwise direction is almost the same as that in the absence of gravity. As noted before, at large shear velocity (greater than 0.3 m/s), the effect of gravity is negligible. The simulation results for $u^* = 0.1$ m/s are shown in Fig. 17(b). It is observed that the effect of gravity in the flow direction is significant, and it makes both spherical and ellipsoidal particles move faster than the case in the absence of gravity.

Figs. 17(c) and (d), respectively, show variations of the RMS fluctuation velocities of ellipsoidal particles and the fluid in different directions near wall for $u^* = 0.3$ and $u^* = 0.1$ m/s. It is observed that the streamwise RMS velocities of ellipsoidal particles are larger than that of the fluid. Both particle and fluid streamwise fluctuation velocities increase sharply up to about 12 wall from the wall and then decrease. The particle RMS velocities in the spanwise direction are slightly smaller than that of the fluid. The v' component of ellipsoids is larger than that of the fluid up to 10 wall units from the wall and then becomes smaller in the outer region. Fig. 17(c) shows that the RMS velocities of ellipsoidal particles are not affected by the presence of gravity in the flow direction for $u^* = 0.3$ m/s. For $u^* = 0.1$ m/s, Fig. 17(d) shows that the particle RMS velocities somewhat increase when the gravity is in the flow direction when compared with the case in the absence of gravity.

7.6. Mean force

To study the magnitude of various forces acting on ellipsoidal particles, additional simulations for $u^* = 0.1$, 0.3 m/s and $S = 1000$ in the absence or presence of gravity are performed. An ensemble of 8192 ellipsoidal particles with $\tau_p^+ = 5, d = 15$ μm for spherical particles, $a = 4.95$ μm, $\beta = 5$ and $a = 4.39$ μm, $\beta = 10$ for ellipsoidal particles for flows with $u^* = 0.3$ m/s are used. For $u^* = 0.1$ m/s, $a = 14.8$ μm for ellipsoidal particles with $\beta = 5$ and $d = 45$ μm for spherical particles are used in the simulation to maintain constant relaxation time of $\tau_p^+ = 5$.

Particles are initially randomly distributed in the region within 30 wall units from the lower wall. At every time step, ensemble averages of the y-component of drag and the lift forces acting on particles that are moving in the region within 12 wall units from the lower wall are computed. (Positive sign denotes that the direction is away from the lower wall.) The simulation results for the time duration of 20–100 wall units are shown in Fig. 18 (i.e., the time after the startup to 20 wall units is omitted to eliminate the effect of initial conditions.)

Fig. 18 shows the variation of mean forces in the y-direction acting on ellipsoids with $\tau_p^+ = 5.0$ and various aspect ratios versus time for different shear velocities. The results for spherical particles are also shown in this figure for comparison. For $u^* = 0.3$ m/s, Fig. 18(a) indicates that the magnitudes of drag and lift forces for ellipsoidal and spherical particles are very similar. As was noted in Fig. 17, ellipsoidal and spherical particles move faster than the fluid in the wall region; therefore, they experience a mean lift force toward the wall. The positive drag force in this figure clearly indicates that there exists a trend of particle migration toward the wall. The results for the case that the gravity is in the flow direction and in the absence of gravity are also shown in this figure. It is observed that the variation of mean forces due to different gravity conditions is negligible at such high shear velocities.

For $u^* = 0.1$ m/s, Fig. 18(b) shows that the magnitudes of mean drag and lift forces are much larger for downward flows (g in flow direction) than those in the absence of gravity. As was noted

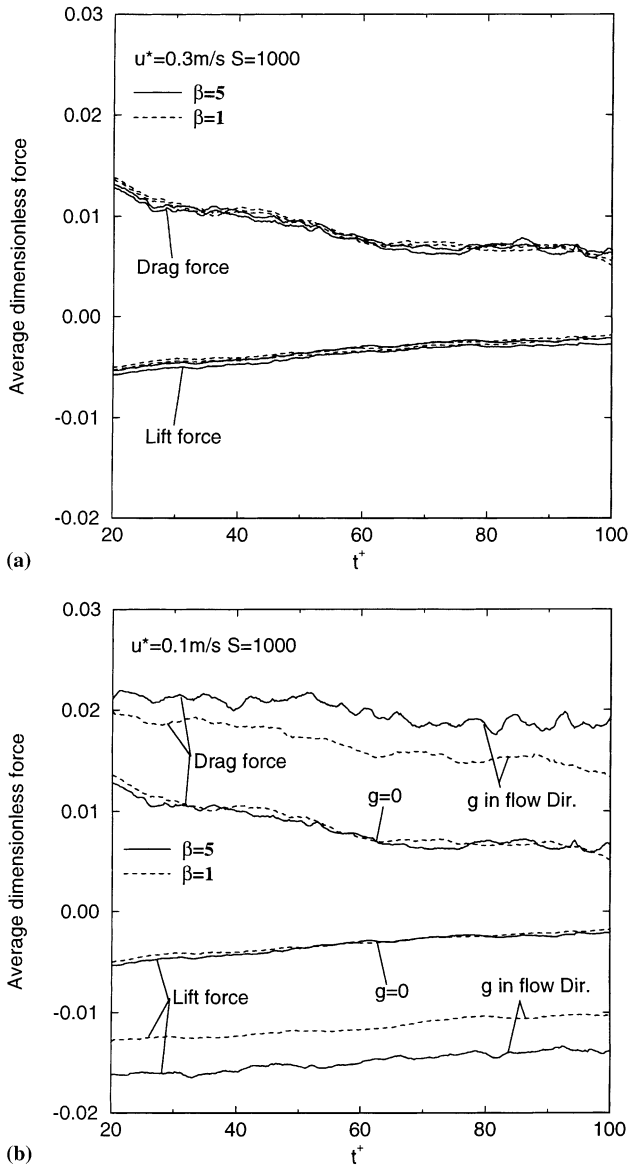

Fig. 18. Time variations of averaged forces in cross stream directions for different aspect ratios and shear velocities: (a) $u^* = 0.3$ m/s; (b) $u^* = 0.1$ m/s.

in Fig. 17(b), the presence of gravity increases the slip velocity of particles (when it is in the flow direction), thus the lift force toward the wall increases. Fig. 18(b) also shows that the magnitudes of mean lift and drag force for ellipsoidal particles are larger than those for spherical particles with the same relaxation time for downward flow conditions. This indicates that the migration toward the wall for ellipsoidal particles is more pronounced than that for spherical particles when gravity is in the flow direction.

8. Conclusions

In this work, the transport and deposition of ellipsoidal particle in a dilute turbulent channel flow under the assumption of one way coupling are studied. The flow field is generated by a direct numerical simulation of the Navier–Stokes equation with the aid of a pseudospectral method. The hydrodynamic drag and torque, the shear-induced lift and gravitational forces are included in the governing equations. Euler's four parameters (also known as quaternions) are used for describing the time evolution of ellipsoidal orientation. The numerical simulation results for various cases are compared with the available experimental data and sublayer model predictions. Based on the results presented, the following conclusions are drawn:

- Both spherical and ellipsoidal particles tend to accumulate in the viscous sublayer and the rate of accumulation in the sublayer increases with the particle aspect ratio.
- The coherent vortical structure of the near wall turbulent flows plays an important role on the ellipsoidal particle transport and deposition processes.
- Ellipsoidal particles tend to accumulate in certain bands with the spacing of about 100–150 wall units due to the turbulent near wall eddy structures.
- Aspect ratio plays an important role in the ellipsoidal particle deposition rate.
- The transport and dispersion of particles with relatively large relaxation times are almost entirely governed by the turbulent flows, and the shape of the particle contributes little to their dispersion process.
- The present DNS simulation results for deposition velocity of ellipsoidal particles are in good agreement with the experimental data, the sublayer model predictions, and empirical equation results.
- As the particle aspect ratio increases, the deposition velocity for $0.5 < \tau_{eq}^{+} < 10$ increases sharply due to the increase in the efficiency of the interception mechanism.
- The effect of particle aspect ratio on deposition velocity is more significant at low shear velocities.
- The effect of gravity on particle deposition velocity strongly depends on the magnitude of flow shear velocity. The nondimensional deposition velocity increases due to the presence of gravity in the flow direction in ducts.
- The gravitational sedimentation enhances the deposition rate on the lower wall in horizontal duct flows. The enhancement effect is significant at low shear velocities of about 0.1 m/s, but becomes small as u^* becomes larger than 0.3 m/s.
- Ellipsoids tend to align themselves with the flow direction.
- Ellipsoidal particles mostly rotate about the z-axis due to the streamwise mean shear field with little rotation about the y-axis perpendicular to the shear field.
- Spherical and ellipsoidal particles generally move faster than the fluid in the streamwise direction. The slip velocity increases when gravity is in the flow direction.
- For vertical ducts, the effect of the presence of gravity along the flow direction on ellipsoids transport and deposition in the viscous sublayer is negligible for flows with high shear velocities, but becomes quite significant at low shear velocities.
- Ellipsoidal particles tend to move toward the wall by experiencing a lift force toward the wall in the wall region. The migration trend increases when gravity is in the flow direction specially for flows with low shear velocities.

- For fixed relaxation time, the wall migration increases with particle aspect ratio particularly for downward flows at low shear velocities.

Acknowledgements

This work was supported by the US Department of Energy (NETL), and the New York STAR through the Center for Advanced Material Processing (CAMP) of Clarkson University. The use of the NSF National Supercomputer Facility of the San Diego University is also gratefully acknowledged.

References

Ahmadi, G., 1993. Overview of digital simulation procedures for aerosol transport in turbulent flows. In: Mittal, K.L. (Ed.), Particle in Gases and Liquids 3: Detection, Characterization, and Control. Plenum, New York, pp. 10–23.

Asgharian, B., Yu, C.P., Gradon, L., 1988. Diffusion of fiber in a tubular flow. Aerosol Sci. Tech. 9, 213–219.

Asgharian, B., Yu, C.P., 1989. Deposition of fibers in the rat lung. J. Aerosol Sci. 20, 355–366.

Brenner, H., 1964. The stokes resistance of an arbitrary particle-IV, Arbitrary fields of flow. Chem. Eng. Sci. 19, 703–727.

Brooke, J.W., Kontomaris, K., Hanratty, T.J., McLaughlin, J.B., 1992. Turbulent deposition and trapping of aerosols at a wall. Phys. Fluids A 4, 825–834.

Chen, Q., Ahmadi, G., 1997. Deposition of particles in a turbulent pipe flow. J. Aerosol Sci. 28, 789–796.

Chen, Y.J., Yu, C.P., 1990. Sedimentation of charged fibers from a two-dimensional channel flow. Aerosol Sci. Tech. 12, 786–792.

Cherukat, P., McLaughlin, J.B., 1990. Wall induced lift on a sphere. Int. J. Multiphase Flow 16, 899–907.

Cleaver, J.W., Yates, B., 1973. Mechanism of detachment of colloid particles from a flat substrate in turbulent flow. J. Colloid Interface Sci. 44, 464–474.

Cleaver, J.W., Yates, B., 1975. A sublayer model for deposition of the particles from turbulent flow. Chem. Eng. Sci. 30, 983–992.

Cleaver, J.W., Yates, B., 1976. The effect of re-entrainment on particle deposition. Chem. Eng. Sci. 31, 147–151.

Einser, A.D., Gallily, I., 1982. On the stochastic nature of the motion of nonspherical aerosol particles IV. General convective rotational velocities in a simple shear flow. J. Colloid Interface Sci. 88, 185–196.

Fan, F.-G., Ahmadi, G., 1993. A sublayer model for turbulent deposition of particles in vertical ducts with smooth and rough surfaces. J. Aerosol Sci. 24, 45–64.

Fan, F.-G., Ahmadi, G., 1995a. Analysis of particle motion in the near-wall shear layer vortices-application to the turbulent deposition process. J. Colloid Interface Sci. 172, 263–277.

Fan, F.-G., Ahmadi, G., 1995b. Dispersion of ellipsoidal particle in an isotropic pseudo-turbulent flow field. ASME J. Fluids Eng. 117, 154–161.

Fan, F.-G., Ahmadi, G., 1995c. A sublayer model for wall deposition of ellipsoidal particles in turbulent streams. J. Aerosol Sci. 26, 813–840.

Fan, F.-G., Ahmadi, G., 2000. Wall deposition of small ellipsoids from turbulent air flows – a Brownian dynamics simulation. J. Aerosol Sci. 31, 1205–1229.

Fan, F.-G., Soltani, M., Ahmadi, G., Hart, S.C., 1997. Flow-induced resuspension of rigid-link fibers from surfaces. Aerosol Sci. Technol. 27, 97–115.

Fichman, M., Gutfinger, C., Pnueli, D., 1988. A model for turbulent deposition of aerosols. J. Aerosol Sci. 19, 123–136.

Foss, J.M., Frey, M.F., Schamberger, M.R., Peters, J.E., Leong, K.M., 1989. Collection of uncharged prolate spherical aerosol particles by spherical collectors. I: 2D motion. J. Aerosol Sci. 20, 515–532.

Galliy, I., Cohen, A.H., 1979. On the orderly nature of the motion of nonspherical aerosol particles. II. Inertial collision between a spherical large droplet and axially symmetrical elongated particle.. J. Colloid Interface Sci. 68, 338–356.

Gallily, I., Eisner, A.D., 1979. On the orderly nature of the motion of non-spherical aerosol particles. I. Deposition from a laminar flow. J. Colloid Interface Sci. 68, 320–337.

Goldstein, H., 1980. Classical Mechanics, 2nd Ed.. Addison-Wesley, Reading, MA.

Gradon, L., Grzybowsk, P., Pilacinsk, W., 1989. Analysis of motion and deposition of fibrous particles on a single filter element. Chem. Eng. Sci. 43, 1253–1259.

Harper, E.Y., Chang, I.D., 1968. Maximum dissipation resulting from lift in a slow viscous shear flow. J. Fluid Mech. 33, 209–225.

Hinch, E.J., Leal, L.G., 1976. Constitutive equations in suspension mechanics. Part 2. Approximate forms for a suspension of rigid particles affected by Brownian rotations. J. Fluid Mech. 76, 187–208.

Hinds, W.C., 1982. Aerosol Technology, Properties, Behavior, and Measurement of Airborne Particles. Wiley, New York (II. The turbulent case. J. Aerosol Sci. 19, 197–211).

Hinze, J.O., 1975. Turbulence. McGraw-Hill, New York.

Hughes, P.C., 1986. Spacecraft Attitude Dynamics. Wiley, New York.

Jeffery, G.B., 1922. The motion of ellipsoidal particles immersed in a viscous fluid. Proc. R. Soc. A 102, 161–179.

Johnson, D.L., Martonen, T.B., 1993. Fiber deposition along airway walls: effects of fiber cross-section on rotational interception. J. Aerosol Sci. 24, 525–536.

Kim, J., Moin, P., Moser, R., 1987. Turbulent statistics in fully developed channel flow at low Reynolds number. J. Fluid Mech. 177, 133–166.

Koch, D.L., Shaqfeh, S.G., 1990. The average rotation rate of a fiber in the linear flow of a semidilute suspension. Phys. Fluids A 2, 2093–2102.

Krushkal, E.M., Gallily, I., 1984. On the orientation distribution function of nonspherical aerosol particles in a general shear flow. I. The laminar case. J. Colloid Interface Sci. 99, 141–152.

Krushkal, E.M., Gallily, I., 1988. On the orientation distribution function of nonspherical aerosol particles in a general shear flow. II. The turbulent case. J. Aerosol Sci. 19, 197–211.

Kulick, J.D., Fessler, J.R., Eaton, J.K., 1994. Particle response and turbulence modification in fully developed channel flow. J. Fluid Mech. 277, 109–134.

Kvasnak, W., Ahmadi, G., 1995. Fibrous particle deposition in a turbulent channel flow: an experimental study. Aerosol Sci. Tech. 23, 641–652.

Li, A., Ahmadi, G., 1993. Deposition of aerosols on surfaces in a turbulent channel flow. Int. J. Eng. Sci. 31, 435–4451.

Massah, H., Kontomaris, K., Schowalter, W.R., Hanrantty, T.J., 1993. The configurations of a FENE bead-spring chain in transient rheological flows and in a turbulent flow. Phys. Fluids A 5, 881–889.

McCoy, D.D., Hanratty, T.J., 1977. Rate of deposition of droplets in annular two-phase flow. Int. J. Multiphase Flows 3, 319–331.

McLaughlin, J.B., 1989. Aerosol particle deposition in numerically simulated turbulent channel flow. Phys. Fluids A 1, 1211–1224.

McLaughlin, J.B., 1991. Inertial migration of a small sphere in linear shear flows. J. Fluid Mech. 224, 261–274.

McLaughlin, J.B., 1993. The lift on a small sphere in wall-bounded linear shear flows. J. Fluid Mech. 246, 249–265.

Ounis, H., Ahmadi, G., McLaughlin, J.B., 1991. Dispersion and deposition of Brownian particles from point sources in a simulated turbulent channel flow. J. Colloid interface Sci. 147, 233–250.

Ounis, H., Ahmadi, G., McLaughlin, J.B., 1993. Brownian particle deposition a directly simulated turbulent channel flow. Phys. Fluids A 5, 1427–1432.

Papavergos, P.G., Hedley, A.B., 1984. Particle deposition behavior from turbulent flows. Chem. Eng. Res. Des. 62, 275–295.

Pedinotti, S., Mariotti, G., Banerjee, S., 1992. Direct numerical simulation of particle behavior in the wall region of turbulent flows in horizontal channels. Int. J. Multiphase Flow 18, 927–941.

Rashidi, M., Hetsroni, G., Banerjee, S., 1990. Particle-turbulence interaction in a boundary layer. Int. J. Multiphase Flow 16, 935–949.

Saffman, P.G., 1965. The lift on a small sphere in a slow shear flow. J. Fluid Mech. 22, 385–400.

Saffman, P.G., 1968. Corrigendum to the lift on a small sphere in a slow shear flow. J. Fluid Mech. 31, 624.
Schamberger, M.R., Peters, J.E., Leong, K.H., 1990. Collection of prolate spherical aerosol particles by charged spherical collectors. J. Aerosol Sci. 21, 539–554.
Schiby, D., Gallily, I., 1980. On the orderly nature of the motion of nonspherical aerosol particles. III. The effect of the particle-wall fluid-dynamic interaction. J. Colloid Interface Sci. 77, 328–352.
Shapiro, M., Goldenberg, M., 1993. Deposition of glass fiber particles from turbulent air flow in a pipe. J. Aerosol Sci. 24, 65–87.
Shaqfeh, S.G., Fredrickson, G.H., 1990. The hydrodynamic stress in a suspension of rods. Phys. Fluids A 2, 7–24.
Smith, C.R., Schwartz, S.P., 1983. Observation of streamwise rotation in the near-wall region of a turbulent boundary layer. Phys. Fluids 26, 641–652.
Soltani, M., Ahmadi, G., 1995. Direct numerical simulation of particle entrainment in turbulent channel flow. Phys. Fluids 7, 647–657.
Soltani, M., Ahmadi, G., 2000. Direct numerical simulation of curly fibers in turbulent channel flow. Aerosol Sci. Tech. 33, 392–418.
Soltani, M., Fan, F.G., Ahmadi, G., Hart, S.C., 1997. Detachment of rigid-link fibers with linkage contact in a turbulent boundary layer flow. J. Adhesion Sci. Tech. 11, 1017–1037.
Squires, K.D., Eaton, J.K., 1991a. Measurements of particle dispersion obtained from direct numerical simulations of isotropic turbulence. J. Fluid Mech. 226, 1–35.
Squires, K.D., Eaton, J.K., 1991b. Preferential concentration of particles by turbulence. Phys. Fluids A 3, 1169–1178.
Wood, N.B., 1981a. A simple method for the calculation of turbulent deposition to smooth and rough surfaces. J. Aerosol Sci. 12, 275–290.
Wood, N.B., 1981b. The mass transfer of particle and acid vapor to cooled surfaces. J. Inst. Energy 76, 76–93.
Zhang, H., Ahmadi, G., 2000. Aerosol particle transport and deposition in vertical and horizontal turbulent duct flows. J. Fluid Mech. 406, 55–80.